Ore Geology Reviews 79 (2016) 1–25

Contents lists available at ScienceDirect

Ore Geology Reviews

journal homepage: www.elsevier.com/locate/oregeorev

# Genesis of the Huangshaping W–Mo–Cu–Pb–Zn polymetallic deposit in Southeastern Hunan Province, China: Constraints from fluid inclusions, trace elements, and isotopes

Li Xiaofeng [a,b,c,*], Huang Cheng [d], Wang Chunzeng [e], Wang Lifa [f]

[a] Key Laboratory of Mineral Resources, Institute of Geology and Geophysics, Chinese Academy of Sciences, Beijing 100029, China
[b] College of Earth Science, University of Chinese Academy of Sciences, Beijing 100049, China
[c] Institute of Geochemistry, Chinese Academy of Sciences, Guiyang 550002, China
[d] Nanchang Institute of Technology, Nanchang 330099, China
[e] University of Maine at Presque Isle, Presque Isle, ME 04769, USA
[f] Huangshaping Mine Company, Chenzhou 424421, China

ARTICLE INFO

*Article history:*
Received 18 January 2016
Accepted 24 April 2016
Available online 29 April 2016

*Keywords:*
W–Mo–Cu–Pb–Zn deposit
Fluid inclusions
Trace elements
Isotopes
Skarn
Huangshaping
South China

ABSTRACT

The Huangshaping polymetallic deposit is located in southeastern Hunan Province, China. It is a world-class W–Mo–Pb–Zn–Cu skarn deposit in the Nanling Range Metallogenic Belt, with estimated reserves of 74.31 Mt of W–Mo ore at 0.28% $WO_3$ and 0.07% Mo, 22.43 Mt of Pb–Zn ore at 3.6% Pb and 8.00% Zn, and 20.35 Mt of Cu ore at 1.12% Cu. The ore district is predominantly underlained by carbonate formations of the Lower Carboniferous period, with stocks of quartz porphyry, granite porphyry, and granophyre. Skarns occurred in contact zones between stocks and their carbonate wall rocks, which are spatially associated with the above-mentioned three types of ores (i.e., W–Mo, Pb–Zn, and Cu ores).

Three types of fluid inclusions have been identified in the ores of the Huangshaping deposit: aqueous liquid–vapor inclusions (Type I), daughter-mineral-bearing aqueous inclusions (Type II), and $H_2O$–$CO_2$ inclusions (Type III). Systematic microthermometrical, laser Raman spectroscopic, and salinity analyses indicate that high-temperature and high-salinity immiscible magmatic fluid is responsible for the W–Mo mineralization, whereas low-temperature and low-salinity magmatic-meteoric mixed fluid is responsible for the subsequent Pb–Zn mineralization. Another magmatic fluid derived from deep-rooted magma is responsible for Cu mineralization.

Chondrite-normalized rare earth element patterns and trace element features of calcites from W–Mo, Pb–Zn, and Cu ores are different from one another. Calcite from Cu ores is rich in heavy rare earth elements (187.4–190.5 ppm), Na (0.17%–0.19%), Bi (1.96–64.60 ppm), Y (113–135 ppm), and As (9.1–29.7 ppm), whereas calcite from W–Mo and Pb–Zn ores is rich in Mn (>10.000 ppm) and Sr (178–248 ppm) with higher Sr/Y ratios (53.94–72.94). $\delta^{18}O$ values also differ between W–Mo/Pb–Zn ores ($\delta^{18}O$ = 8.10‰–8.41‰) and Cu ores ($\delta^{18}O$ = 4.34‰–4.96‰), indicating that two sources of fluids were, respectively, involved in the W–Mo, Pb–Zn, and Cu mineralization.

Sulfur isotopes from sulfides also reveal that the large variation (4‰–19‰) within the Huangshaping deposit is likely due to a magmatic sulfur source with a contribution of reduced sulfate sulfur host in the Carboniferous limestone/dolomite and more magmatic sulfur involved in the Cu mineralization than that in W–Mo and Pb–Zn mineralization. The lead isotopic data for sulfide (galena: $^{206}Pb/^{204}Pb$ = 18.48–19.19, $^{207}/^{204}Pb$ = 15.45–15.91, $^{208}/^{204}Pb$ = 38.95–39.78; sphalerite: $^{206}Pb/^{204}Pb$ = 18.54–19.03, $^{207}/^{204}Pb$ = 15.60–16.28, $^{208}/^{204}Pb$ = 38.62–40.27; molybdenite: $^{206}Pb/^{204}Pb$ = 18.45–19.21, $^{207}/^{204}Pb$ = 15.53–15.95, $^{208}/^{204}Pb$ = 38.77–39.58 chalcopyrite: $^{206}Pb/^{204}Pb$ = 18.67–19.38, $^{207}/^{204}Pb$ = 15.76–19.90, and $^{208}/^{204}Pb$ = 39.13–39.56) and oxide (scheelite: $^{206}Pb/^{204}Pb$ = 18.57–19.46, $^{207}/^{204}Pb$ = 15.71–15.77, $^{208}/^{204}Pb$ = 38.95–39.13) are different from those of the wall rock limestone ($^{206}Pb/^{204}Pb$ = 18.34–18.60, $^{207}/^{204}Pb$ = 15.49–15.69, $^{208}/^{204}Pb$ = 38.57–38.88) and porphyries ($^{206}Pb/^{204}Pb$ = 17.88–18.66, $^{207}/^{204}Pb$ = 15.59–15.69, $^{208}/^{204}Pb$ = 38.22–38.83), suggesting $Pb^{206}$-, $U^{238}$-, and Th $^{232}$-rich material are involved in the mineralization. The Sm–Nd isotopes of scheelite ($\varepsilon_{Nd}(t)$ = −6.1 to −2.9), garnet ($\varepsilon_{Nd}(t)$ = −6.8 to −6.1), and calcite ($\varepsilon_{Nd}(t)$ = −6.3) from W–Mo ores as well as calcite ($\varepsilon_{Nd}(t)$ = −5.4 to −5.3) and scheelite ($\varepsilon_{Nd}(t)$ = −2.9) from the Cu ores demonstrate suggest more mantle-derived materials involved in the Cu mineralization.

* Corresponding author.
*E-mail address:* xiaofengli@mail.iggcas.ac.cn (L. Xiaofeng).

http://dx.doi.org/10.1016/j.oregeorev.2016.04.023

In the present study we conclude that two sources of ore-forming fluids were involved in production of the Huangshaping W–Mo–Pb–Zn–Cu deposit. One is associated with the granite porphyry magmas responsible for the W–Mo and then Pb–Zn mineralization during which its fluid evolved from magmatic immiscible to a magmatic–meteoritic mixing, and the other is derived from deep-rooted magma, which is related to Cu-related mineralization.



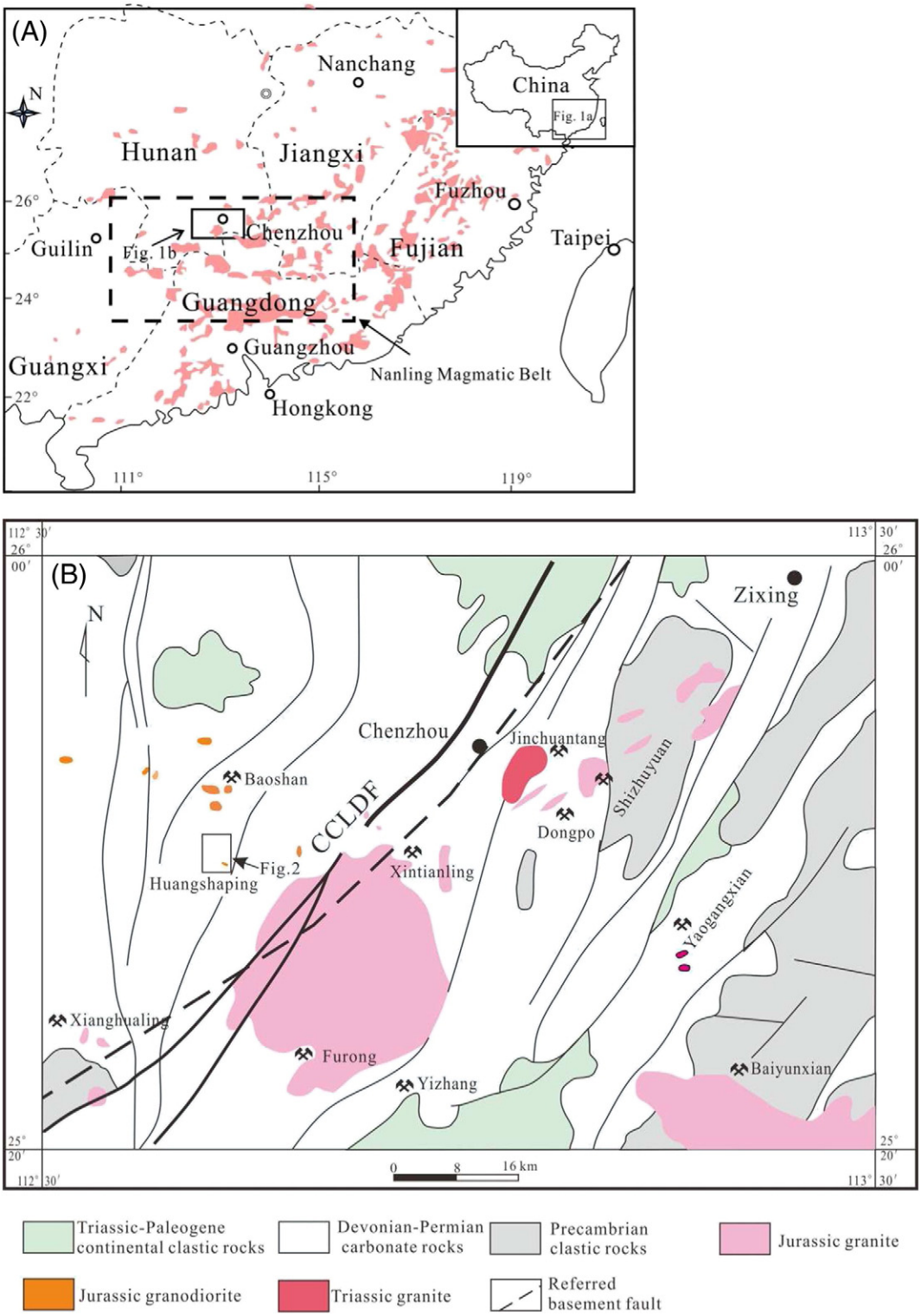


**Fig. 1.** (A) Location of the southeast Hunan polymetallic mineralization district in the Nanling Magmatic Belt. (B) Simplified regional geologic map of the district (modified after Southeast Hunan Geological Team (1991), unpublished). CCLDF refers to the Chaling–Chenzhou–Linwu Deep Fault Zone.

## 1. Introduction

Southeastern Hunan Province, which is located in the western section of the Nanling Magmatic Belt in South China, is a well-known polymetallic mineralization district (Fig. 1). The district includes a number of world-class or super-large ore deposits of nonferrous and rare metals (e.g., the Shizhuyuan W–Sn–Mo–Bi, Furong Sn, Xintianling W, Yaogangxian W, Xianghualing Sn and rare-metal, Shuikoushan Pb–Zn, Baoshan Pb–Zn–Cu, and Huangshaping W–Mo–Cu–Pb–Zn deposits). These polymetallic deposits are generally classified into two metallogenic systems: a W–Sn–Mo–Bi system and a Pb–Zn–Ag–Cu system (Bai et al., 2007). Deposits of these two systems are distributed on both sides of the regional NNE-striking Chaling–Chenzhou–Linwu Deep Fault Zone (CCLDF; Fig. 1B). The Shizhuyuan, Furong, Xintianling, and Yaogangxian deposits of the W–Sn–Mo–Bi system mainly occur on the southeast side of the CCLDF, whereas the Shuikoushan, Baoshan, and Huangshaping deposits of the Pb–Zn–Ag–Cu system are distributed on the northwest side of the CCLDF (Table 1; Fig. 1B). These two metallogenic systems are related to different granitoids, respectively (Zhai et al., 1999; Bai et al., 2007). The higher temperature W–Sn–Mo–Bi mineralization system is related to S-type granitoids in the SE side whereas the lower temperature Pb–Zn–Ag–Cu mineralization system is related to I-type granitoids in the NW side. Some researchers have addressed other factors that could control formation of these two mineralization systems, for example, the geochemical composition of host rocks, faults and folds, the thickness of the lithosphere, the intensity of deep-seated thermal perturbations, the scale of magmatism, and the emplacement depth of magmas (Zhang et al., 2000; Bai et al., 2007, 2008).

The Huangshaping deposit was first mined as a Pb–Zn deposit back in the Tang Dynasty (about 700 CE), whereas modern industrial mining of this historical deposit started in 1967. The deposit has produced 16.75 Mt of ore with grades of 3.71 wt% for Pb, 8.21 wt% for Zn, and 1.36 wt% for Cu, as well as some Sn and Fe from the skarn and vein-type orebodies. From 2007 a new round of intensive exploration was conducted and numerous skarn-type W–Mo and Cu orebodies were discovered beneath the Pb–Zn orebodies at deeper levels (Fig. 2). The total ore reserve of the deposit hence increased to 74.31 Mt of W–Mo ore at 0.28 wt% $WO_3$ and 0.07 wt% Mo, 5.68 Mt of Pb–Zn ore at 3.36 wt% Pb and 7.21 wt% Zn, and 3.60 Mt of Cu ore at 1.02 wt% Cu (Southeast Hunan Geological Team, 2011, unpublished report).

Since the 1970s, numerous investigations and research activities have been undertaken on the Huangshaping polymetallic deposit, including studies of mine geology (Wang et al., 1993; Zhu et al., 1995; Deng, 1997; Huang, 1999), ore genesis (Gu, 1997; Li, 1997; Shen, 1999), ore-controlling structures (Li, 1997), and ore geochronology (Yao et al., 2005, 2007; Ma et al., 2007; Lei et al., 2010; Qi et al., 2012). A general consensus has been reached among the researchers that the deposit has a close genetic relationship to magmatic–hydrothermal activities of the Late Jurassic granite porphyry and quartz porphyry intrusions and that it is a typical skarn polymetallic deposit (Zhong, 1996; Gu, 1997; Shen, 1999; Zeng, 2001). The deposit contains three types of ores: skarn type W–Mo, vein-type Pb–Zn, and vein-type Cu. However, some unresolved questions remain: For example, did three types of orebody precipitate from a single source of ore-forming fluids or from multiple sources superimposed upon one another? What was the origin and evolution of ore-forming fluids associated with, respectively, W–Mo, Pb–Zn, and Cu mineralization?

In this paper we present a detailed study of fluid inclusions, S and Pb isotopes of sulfides, O isotopes of scheelite, C and O isotopes and trace elements of gangue minerals (mainly fluorite and calcite), and Sm–Nd isotopes of W–Mo, Pb–Zn, and Cu ores from the deposit. The study is aimed at addressing the above questions and improving our understanding of sources and evolution of the ore-forming fluids in the Huangshaping polymetallic deposit.

**Table 1**
Summary of geology and mineralogy of representative deposits in the Southeastern Hunan Mineral District.

| Deposit | Host rock | Styles of mineralization | Ages of related granite (Ma) | Age of mineralization (Ma) | Gangue minerals | Ore minerals | References |
|---|---|---|---|---|---|---|---|
| Shuikoushan | Middle-Permian carbonaceous limestone, marl, and shale | Skarn Pb-Zn, layered lenticular Pb-Zn-Cu | 162.8 ± 0.7, 156.6 ± 0.4 (zircon LA-ICP-MS U-Pb) | 163 ± 2 (molybdenite Re-Os) | Garnet, diopside, wollastonite, actinolite, and quartz | Magnetite, pyrite, sphalerite, galena, wolframite, and chalcopyrite | Ma et al. (2006a, 2006b) |
| Baoshan | Lower-Carboniferous dolomitic limestone | Skarn Cu-Mo and vein-type Pb-Zn | 164 ± 1.9 (zircon SHRIMP U-Pb) | 160 ± 2 (molybdenite Re-Os) | Garnet, diopside, calcite, fluorite, and quartz | Chalcopyrite, molybdenite, bismuthinite, scheelite, sphalerite, and galena | Lu et al. (2006) Xie et al. (2013) |
| Huangshaping | Lower-Carboniferous limestone and shale | Skarn W-Mo, vein-type Pb-Zn and skarn vein-type Cu | 161.6 ± 1.1 (zircon LA-ICP-MS U-Pb) | 154.8 ± 1.9 (molybdenite Re-Os) | Garnet, diopside, actinolite, vesuvianite, calcite, quartz, fluorite, and sericite | Galena, sphalerite, chalcopyrite, scheelite, molybdenite, magnetite, pyrrhotite, and pyrite | Yao et al. (2005) |
| Shizhuyuan | Upper-Devonian carbonate rocks | Skarn W-*Sn*-Mo-Bi, greisen W, and vein-type Pb-Zn | 152 ± 9 (zircon SHRIMP U-Pb) | 151.1 ± 3.5 (molybdenite Re-Os) | Garnet, vesuvianite, quartz, topaz, and fluorite | Scheelite, wolframite, cassiterite, molybdenite, bismuthinite, stannite, galena, sphalerite, and chalcopyrite | Mao et al. (1996) |
| Xintianling | Carboniferous limestone | Skarn W and vein-type W | 160 ± 2 (zircon LA-ICP-MSU-Pb) | 159.1 ± 1.9 (molybdenite Re-Os) | Garnet, diopside, vesuvianite, quartz, calcite, chlorite, fluorite, tourmaline, and sericite | Scheelite, molybdenite, bismuthinite, cassiterite, and pyrrhotite | Cai et al. (2008) |
| Furong | Permian carbonate rocks | Skarn Sn and greisen Sn | 157.5 ± 0.3 (zircon LA-ICP-MS U-Pb) | 156.1 ± 0.4 (molybdenite Re-Os) | Garnet, diopside, calcite, quartz, fluorite, sericite, and chlorite | Magnetite, cassiterite, pyrite, chalcopyrite, tetrahedrite, galena, acanthite, chalcocite, and argyrite | Mao et al. (2004) |
| Xianhualing | Devonian dolostone | Skarn Sn | 159 (zircon LA-ICP-MS U-Pb) | 157–156 (cassiterite U-Pb) | Garnet, diopside, spinel, topaz, fluorite, quartz, and zinnwaldite | wolframite, scheelite, cassiterite, magnetite, arsenopyrite, chalcopyrite, sphalerite, and galena | Bai et al. (2008) |

## 2. Regional geology

The Huangshaping W–Mo–Pb–Zn–Cu polymetallic deposit is located on the NW side of the NNE-striking CCLDF (Fig. 1B). The CCLDF is an overthrust fault zone obducted by the Wugongshan–Zhuguangshan block from SE to NW during the Early Paleozoic (Yao et al., 1993, 2012; Gilder et al., 1996; Wang and Shen, 2003). Some authors (e.g., Yang et al., 2009) have suggested that the deep fault zone acted as a collisional amalgamation zone between the Yangtze block and Cathaysia block during the Early Paleozoic Guangxi'an Orogeny in South China.

The stratified rocks exposed in the region mainly include two types: clastic rocks of marginal-trough basin facies aged from Sinian to Silurian and carbonate rocks of shallow marine platform facies aged from Devonian to Middle Triassic. The Lower Paleozoic sedimentary rocks were slightly metamorphosed and moderately folded during the Guangxi'an Orogeny. A number of E- and NE-striking faults were produced during and after the Orogeny. The subsequent Indosinian Orogeny of the

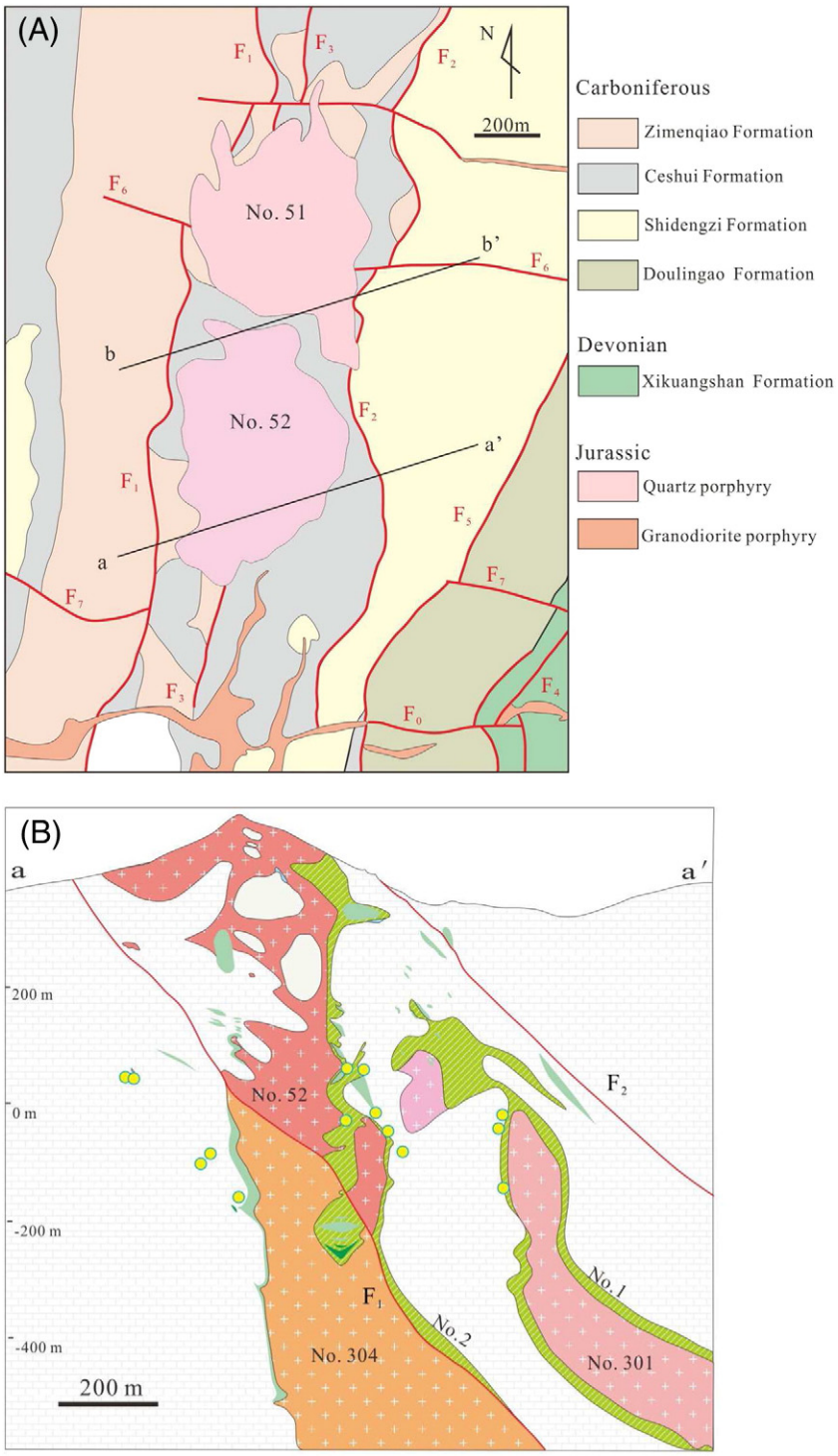


**Fig. 2.** Simplified geologic map of the Huangshaping deposit showing the locations of the samples (A) and cross section along exploration lines (B, C) (modified after Southeast Hunan Geological Team (1991), unpublished).

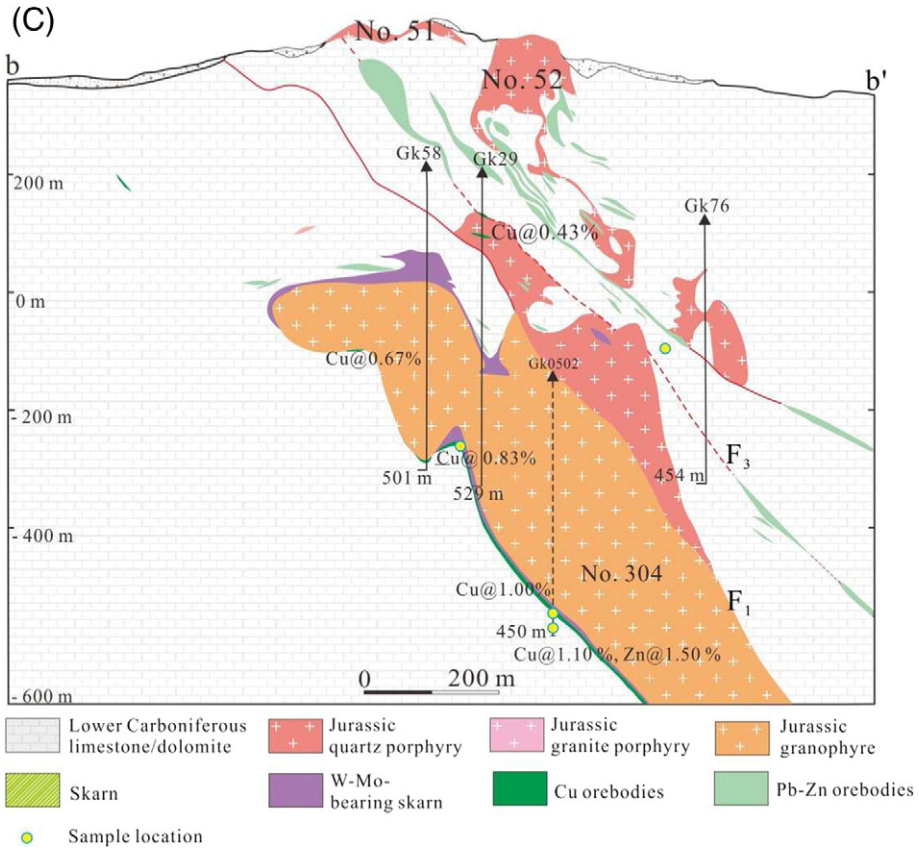


**Fig. 2** (*continued*).

Early Mesozoic produced N-trending folds, which were in turn overprinted by NNE-trending rift basins and large-scale faults during the Late Mesozoic Yanshanian Orogeny (Liu et al., 2005).

Voluminous granitic magmas were generated and emplaced in northeast Hunan Province, and large-scale W–Sn–Mo–Cu–Pb–Zn mineralization occurred during the Yanshanian period of the Middle Jurassic, possibly as a result of subduction of the Farallon–Izanagi mid-ocean-ridge and related transform faults (Bai et al., 2007; Li and Sasaki, 2007; Li et al., 2008; Li et al., 2013a, 2013b, 2013c) (Fig. 1B). On the SE side of the CCLDF, several hypabyssal A-type or S-type plutons, including biotite monzogranite, mica monzogranite, and potassium feldspar granite, are exposed in the uplifted area (T.Q. Ma et al., 2005, 2006a, 2006b; Ma et al., 2006c; Jiang et al., 2006). On the NW side of the CCLDF, a scattered number of small granodiorite porphyry stocks occur (e.g., those of the Baoshan deposit and the Shuikoushan deposit); these have an I-type affinity, suggesting that they were probably derived from enriched lithospheric mantle or asthenospheric mantle with involvement of crustal contamination (Wang et al., 2001; Wu et al., 2005). Although the Huangshaping polymetallic deposit is located on the NW side of the CCLDF, its ore-related granitoids (mainly biotite monzogranite, quartz porphyry, and granite porphyry stocks) are not of typical I-type affinity. On the contrary, their geochemical features are considerably different from those of Baoshan and Shuikoushan granodiorites, being more similar to the granitic rocks of the Qianlishan and Qitianling plutons that occur on the SE side of the CCLDF (Yao et al., 2005).

## 3. Geology of the Huangshaping deposit

### 3.1. Ore deposit geology

Exposed sedimentary rocks in the Huangshaping area (Fig. 2A) include two Devonian formations and four Carboniferous formations. The two Devonian formations are the Shetianqiao Formation, consisting of dolomitic limestone with argillaceous limestone, and the Xikuangshan Formation, consisting of dolomitic limestone, calcareous sandstone, fine sandstone, and shale. The four Carboniferous formations include the Douling Formation, consisting of limestone and dolomitic limestone; the Shidengzi Formation, consisting of limestone with thin-layered carbonaceous mudstone and bioclastic limestone; the Ceshui Formation, consisting of thick-bedded calcareous sandstone, quartz sandstone, and sandy shale; and the Zimenqiao Formation, consisting of dolostone (Fig. 2A).

The Late Jurassic felsic intrusions of the Huangshaping deposit were emplaced in cores of the folds and along faults; they include granodiorite porphyry, quartz porphyry, granite porphyry, and granophyre (Fig. 2A–C). Granodiorite porphyry is porphyritic and contains about 15% phenocrysts, including alkali feldspar, plagioclase, quartz, and biotite. Its groundmass is composed predominantly of felsic feldspars, quartz, biotite, and hornblende. Quartz porphyry is porphyritic and consists of phenocrysts of quartz (6%) and feldspars (4%) and a groundmass of felsitic quartz and feldspars. The granite porphyry is also porphyritic and composed of phenocrysts (25%–43%) of predominantly alkali feldspar, quartz, and minor amounts of plagioclase and biotite, within a matrix of fine-grained quartz and feldspar. The granophyre has a typical granophyric texture and consists of 8%–15% phenocrysts of mostly alkali feldspar (50%–60%) and quartz (35%–40%) and a micrographic groundmass of feldspars and quartz.

Two quartz porphyry stocks (No. 51 and No. 52) were emplaced along fault $F_1$ (Liu et al., 2005) in the north, while a granodiorite porphyry stock (No. 54) intruded along fault $F_0$ in the south. A granophyre stock (No. 304) and a granite porphyry stock (No. 301) are not exposed but encountered in drill holes (Fig. 2B). The No. 301 granite porphyry occurs above the fault $F_1$ (Fig. 2B), whereas the No. 304 granophyre is beneath the fault $F_1$. A potassic microgranite porphyry was also encountered by drilling at a depth of 1000 m, yet its shape and size are still

unclear (Lei et al., 2010; Zhu et al., 2010). The potassic microgranite porphyry is porphyritic and consists of phenocrysts of alkali feldspar (3%–4%), quartz (3%), and plagioclase (1%) and a very fine-grained (at 0.05 mm) groundmass of alkali feldspar (55%–60%), quartz (30%), and plagioclase (5%–10%). Compared to the No. 301 granite porphyry, the No. 304 granophyre shows potassium enrichment and sodium depletion (Deng, 1997).

### 3.2. Geochronology

Age data of granitic rock and ore collected in many previous studies are listed in Table 2. LA-ICP-MS zircon U–Pb dating yielded weighted mean $^{206}Pb/^{238}U$ ages of 158.5 ± 0.9 and 159.1 ± 0.5 Ma for the granodiorite porphyry, 154.9 ± 4.2 Ma for the quartz porphyry, and 161.6 ± 1.1 and 155.2 ± 0.4 Ma for the granite porphyry (Yao et al., 2005; Ma et al., 2007; Yuan et al., 2014; Huang et al., 2013). SHRIMP zircon U–Pb dating yielded similar ages (i.e., 160.8 ± 1.0 and 152.0 ± 3.0 Ma, for the quartz porphyry (Lei et al., 2010; Yuan et al., 2014)). These geochronological data indicate that the quartz porphyry and granite porphyry emplaced during the same magmatic pulse at ~155 Ma, following the granodiorite porphyry that emplaced at ~160 Ma.

As shown in Table 2, molybdenite samples collected from the W–Mo-bearing skarns gave a range of weighted mean Re–Os ages of 153.8 ± 4.8 to 159.1 ± 3.3 Ma with a peak of ~155 Ma (Yao et al., 2007; Ma et al., 2007; Lei et al., 2010; Huang et al., 2013). The 155 Ma peak age is coeval with the zircon U–Pb ages of the quartz porphyry and granite porphyry, suggesting a close temporal relationship between the W–Mo mineralization and emplacement of the porphyries in the Huangshaping deposit.

### 3.3. Skarn mineralogy and mineralization

The Huangshaping deposit is characterized by typical calc-silicate skarns of prograde garnet, hedenbergite, vesuvianite, and diopside, together with retrograde actinolite, tremolite, epidote, and chlorite. The endoskarn occurs near the contacts with granite porphyry, quartz porphyry, and granophyre intrusions. Based on previous work (e.g., Tong et al., 1986; Deng, 1997) and field investigation and ore microscopic and petrographic observations in this study, three types of skarns that relate to W–Mo–Pb–Zn mineralization have been recognized and a detailed paragenetic sequence of the mineralization has been constructed (Fig. 3).

The main features of three types of skarns are as follows: (1) The magnetite–hedenbergite skarn (Fig. 4A and B) consists of hedenbergite, magnetite, and fluorite, with iron-rich riebeckite. Hedenbergite is prismatic and up to 0.4 mm long. (2) The diopside–vesuvianite–garnet skarn (Fig. 4C and D) consists of garnet (grossular), vesuvianite, and diopside with variable amounts of magnetite. Garnet shows a zonation pattern and twins. Most of the garnet crystals are homogeneous, but only some exhibit microscopic homogeneity. Garnet is locally replaced by carbonate minerals as a result of hydrothermal activity. Diopside occurs as stubby equant crystals with sizes of 0.1–0.2 mm. It may present as bands within hessonite. (3) Diopside skarn (Fig. 4E) is a single-mineral skarn, consisting essentially of fibrous diopside. The retrograde skarn minerals of tremolite, actinolite, biotite, and phlogopite usually replace the diopside where molybdoscheelite and cassiterite occur.

There exists a skarn zonation at the deposit. The zonation is centered in the granite porphyry and gradually changes toward its carbonate country rock. For example, at 273 m asl (above sea level), the skarn zonation is centered in the No. 301 granite porphyry (Fig. 5) and shows the following sequence toward the country rock: altered granite porphyry → magnetite–hedenbergite skarn → diopside–garnet skarn → garnet-bearing marble → marble → limestone.

The Huangshaping deposit also shows a vertical mineralization zonation pattern (Fig. 2C and Fig. 6A–I). The upper zone, where the major Pb–Zn ore reserve of the deposit is located, consists of veinlet galena and sphalerite and is capped by sandstone, mudstone, or quartz porphyry. The base of the upper zone (within skarnized limestone) contains veinlet- and skarn-type marmatite, galena, and arsenopyrite. The upper middle zone has skarn-type magnetite, cassiterite, and fluorite. The middle zone (0 to −400 m asl) is composed of skarn-type scheelite, molybdenite, and magnetite. The lower middle zone (−400 to −800 m asl) contains skarn-type scheelite, molybdenite, and bismuthinite. The skarn- and vein-type Cu ores occur mainly at −200 to −900 m asl. Below −400 m asl Cu orebodies dominate the No. 304 granophyre contact zone. Copper orebodies mostly occur within contact zones and sandstone–shale skarn of the Ceshui Formation (Fig. 2C).

Pb–Zn mineralization is closely and spatially associated with the quartz porphyry and granite porphyry intrusions. Pb–Zn ores occur as veins within skarns but predominantly in the Lower Carboniferous limestone (Figs. 2B and C and 6A–C). Their major ore minerals are sphalerite, galena, chalcopyrite, and pyrrhotite.

W–Mo mineralization mainly occurs within skarns at contact zones between the granite porphyry intrusions and their wall rocks and generally in two ore clusters, i.e., clusters No. 1 and No. 2 (Figs. 2B and 6D–F). Ore cluster No. 1, which hosts 89% of the total W–Mo reserve of the deposit, occurs within skarns of contact zone between the No. 301 granite porphyry and limestone of the Shidengzi Formation (Fig. 2B). Orebodies in this cluster are lenticular and stratiform in shape, being 800–1000 m long and 60–400 m wide. They dip toward the SE at a dipping angle of 25°–70°, conformable with the skarn bodies. The ore grades of $WO_3$, Mo, Bi, and Sn in ore cluster No. 1 are 0.25%, 0.06%, 0.07%, and 0.18%, respectively. Ore cluster No. 2 occurs in contact zones between the granophyre–quartz porphyry stock (No. 304) and its wall rocks in the east. The orebodies are in veinlet or lenticular forms with lengths up to 700 m and dip toward the SE at dipping angles of 70°–90°. Quartz–molybdenite veins also occur inside the stock (Fig. 6G). Skarn minerals are predominantly garnet, actinolite, epidote,

**Table 2**
Zircon U-Pb and Molybdenite Re-Os age data of the Huangshaping W-Mo-Cu-Pb-Zn polymetallic deposit.

| Method | Zircon $^{206}Pb/^{238}U$ age SHRIMP | Zircon $^{206}Pb/^{238}U$ age LA-ICP-MS | Molybdenite Re-Os |
|---|---|---|---|
| Granodiorite porphyry | | 158.5 ± 0.9 Ma (Yuan et al., 2014)<br>159.1 ± 0.5 Ma (Huang et al., 2013) | |
| Quartz porphyry | 152.0 ± 3.0 Ma (Lei et al., 2010)<br>160.8 ± 1.0 Ma (Yuan et al., 2014) | 154.9 ± 4.2 Ma (Ma et al., 2007) | |
| Granite porphyry | | 161.6 ± 1.1 Ma (Yao et al., 2005)<br>155.2 ± 0.4 (Yuan et al., 2014) | |
| Mo-bearing ore | | | 154.8 ± 1.9 Ma (Yao et al., 2007) |
| W-Mo-bearing skarn | | | 153.8 ± 4.8 Ma (Ma et al., 2007) |
| W-Mo-bearing skarn | | | 157.6 ± 2.3 Ma; 157.5 ± 2.1 Ma (Lei et al., 2010) |
| Mo-bearing ore | | | 157.6 ± 1.2 Ma (Wang et al., 2010) |
| W-Mo-bearing skarn | | | 158.4 ± 1.3 Ma (Qi et al., 2012) |
| Mo-bearing quartz vein | | | 153.2 ± 1.2 Ma (Huang et al., 2013) |

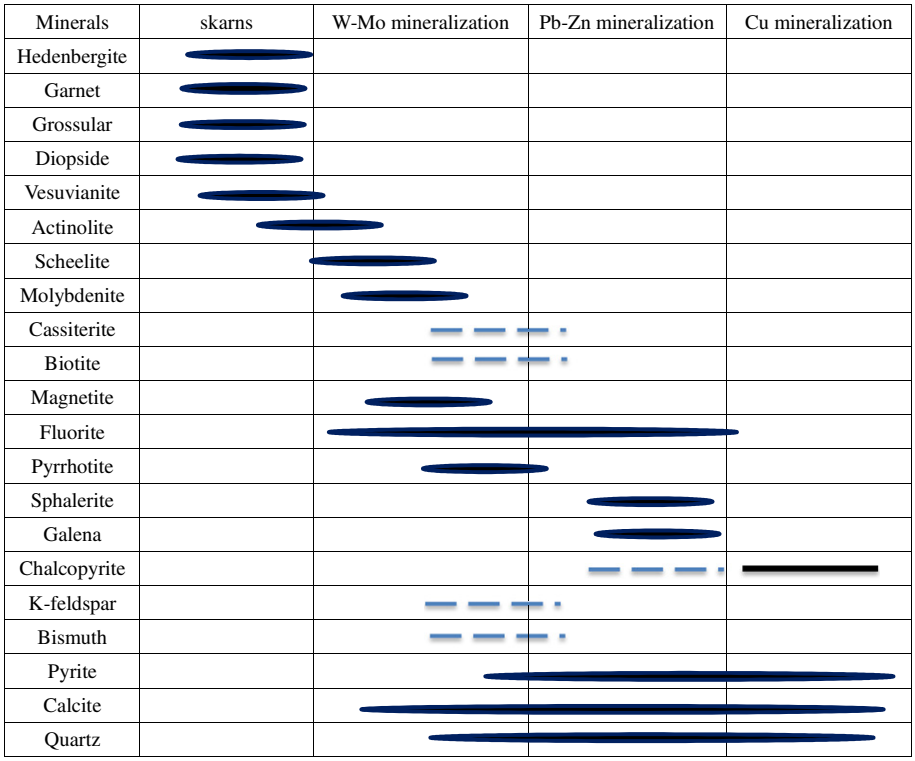


**Fig. 3.** Paragenetic sequence of W–Mo–Pb–Zn–Cu mineralization in the Huangshaping polymetallic skarn deposit.

tremolite, fluorite, and quartz (Fig. 7A–C) and ore minerals include magnetite, scheelite, molybdenite, cassiterite, and bismuthinite in both clusters (Fig. 7A–C).

Copper orebodies were encountered in drill holes in the north of the Huangshaping deposit. They occur within skarns in contact zones between granophyre and limestone or as veins in the limestone (Figs. 2C and 6H and I). Twelve Cu orebodies occur in the skarn zone of granophyre and in the silicified limestone. The orebodies appear as vein-like, lensoidal, or lenticular. Their average thickness is 4.46 m and their average grade is 0.84% for Cu, 1.32% for Pb, and 3.9% for Zn. The largest orebody (No. 580) has a northward strike and dips toward the east at a dipping angle of 50°–80°. The major ore minerals of Cu ore are chalcopyrite, sphalerite, and galena (Fig. 7B and D–H).

Calcite and fluorite are the major gangue minerals in the Pb–Zn, W–Mo, and Cu orebodies. Fluorite exists in purple and green color or is colorless. In general, the purple fluorite is associated with W–Mo ores, the green fluorite with Pb–Zn ores, and the colorless fluorite with both (Fig. 8A–D).

## 4. Sampling and analytical methods

### 4.1. Sample collection

Samples used for analysis in this study were collected from underground galleries within the Huangshaping deposit and boreholes dug into the deposit. Transparent or translucent mineral samples of garnet, actinolite, scheelite, fluorite, quartz, and calcite collected at elevations between 92 to −520 m asl were used for fluid inclusion microthermometry and Raman analyses. Fluorite samples in different colors collected separately from W–Mo, Pb–Zn, and Cu ores and calcite samples collected separately from W–Mo and Cu ores were used for trace elements and Sm–Nd–Pb isotopic analyses. Sulfide minerals of chalcopyrite, pyrite, galena, and sphalerite from different types of ores were collected for S and Pb isotopic analysis. Garnet and scheelite were also used for Sm–Nd and O isotopic analyses.

### 4.2. Fluid inclusions

Fluid inclusions were examined and analyzed from ore and gangue minerals, including garnet, actinolite, calcite, molybdoscheelite, fluorite from skarn and W–Mo ores, quartz from quartz–molybdenite veins, calcite and fluorite from Cu and Pb–Zn ores, and scheelite and calcite from calcite + scheelite + chalcopyrite veins.

Twenty doubly polished thin sections of 0.3–0.5 mm thick were prepared for fluid inclusion petrographic and microthermometric analyses. Microthermometric analysis was performed on a Linkham THMSG 600 computer-controlled freezing-heating stage at the State Key Laboratory of Ore Deposit Geochemistry, Institute of Geochemistry, Chinese Academy of Sciences. Liquid nitrogen was used as a cooling agent. Temperature was measured with a chromel-alumel thermocouple. The sample stage was connected to a thermal control unit (whose temperature range is −196 °C to +600 °C). The stage was periodically calibrated using the boiling point of pure liquid nitrogen (−195.798 °C), the triple point of pure $CO_2$ (−56.6 °C), the ice melting point in a standard NaCl solution (from −18 °C to −1 °C), and the melting points of $AgNO_3$ (210 °C), $K_2CrO_7$ (398 °C), and NaI (651 °C). The measurements were considered accurate to ±0.2 °C for ice-melting and $CO_2$ homogenization temperatures, ±0.5 °C for clathrate melting temperatures, ±1.5 °C for eutectic temperatures, and ±5 °C for homogenization temperatures. The heating rate (at above 30 °C) was 5 °C/min up to a heating limit at 650 °C. The salinity of liquid–vapor inclusions that formed clathrates upon cooling was estimated by using the computing program ICE (Bakker, 1997). The salinity of $CO_2$-bearing inclusions that did not form clathrates upon cooling was estimated by using the technique of Hedenquist and Henley (1985). The salinities of inclusions containing halite, liquid and vapor at room temperature were estimated by using the data and methodology of Bodnar and Vityk (1994). For inclusions that homogenize by halite dissolution, this method underestimates salinity by up to 3 wt% NaCl equiv. (Bodnar and Vityk, 1994). The salinity in liquid–vapor inclusions that contain no $CO_2$ was estimated by using the data of Bodnar (1993).

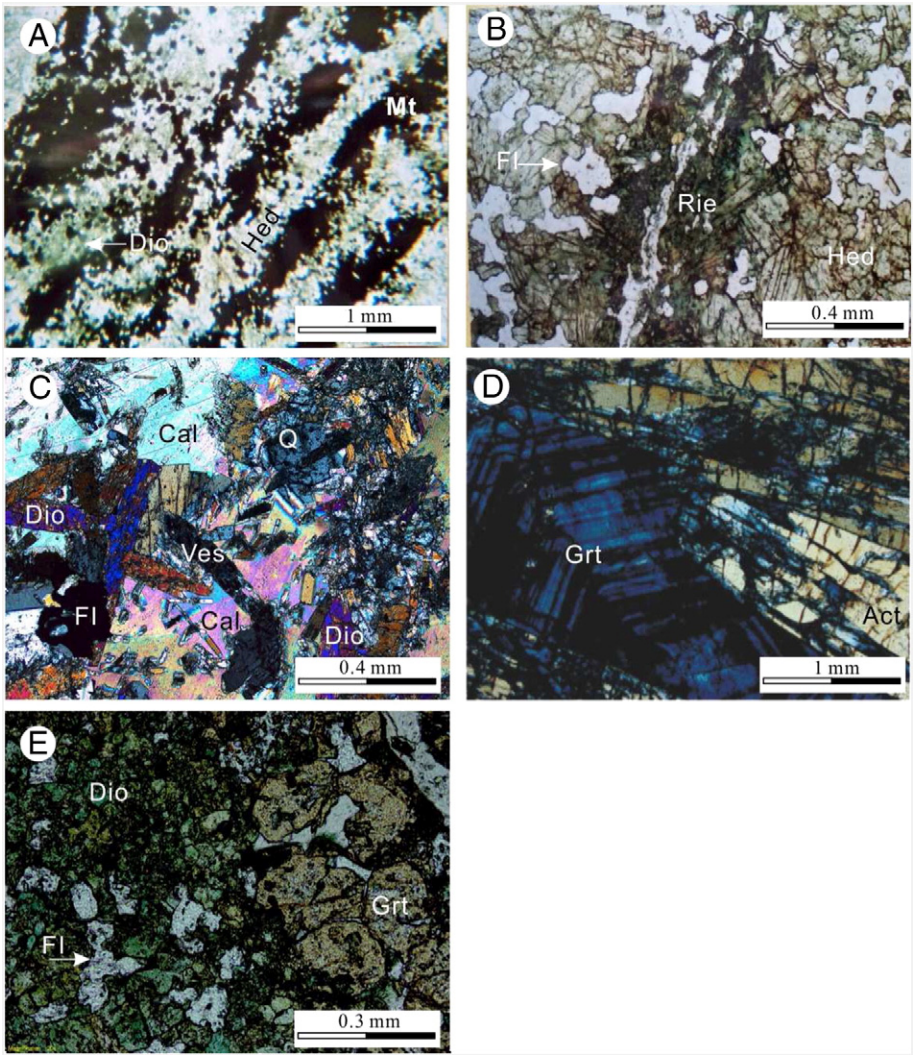


**Fig. 4.** Skarn and skarn minerals from the Huangshaping deposit. (A) Hedenbergite–diopside skarn and banded hedenbergite, diopside, and magnetite. (B) Hedenbergite skarn. Skarn was truncated by an iron-rich riebeckite vein. Hedenbergite was replaced by fluorite. (C) Diopside–vesuvianite skarn. (D) Garnet–actinolite skarn. (E) Diopside–garnet skarn with fluorite. Abbreviations: Act = actinolite, Cal = calcite, Di = diopside, Fl = fluorite, Gar = Garnet, Heden = Hedenbergite, Mt = magnetite, Ves = vesuvianite, Rie = riebeckite.

Laser Raman spectroscopic analysis of single-fluid inclusions was performed with a confocal Renishaw InVia Reflex Raman spectrometer. A Spectra-Physics argon-ion laser was used to excite the laser Raman spectra using a 514-nm laser line at an incident power of 20 mW with 1–2 μm spatial resolution and 60-s integral time.

### 4.3. Trace elements

Fluorite and calcite samples were dissolved in a closed dissolver with a mixture of hydrofluoric and nitric acids and evaporated on an electric hot plate. The samples were dissolved with nitric acid in a hermetically sealed system, then diluted, and directly measured on an ICP-MS by using an external standard method. The analyses were performed at Activation Laboratories Ltd. (Actlabs) (Ancaster, Ontario, Canada).

### 4.4. Stable isotopes

Oxygen was liberated from scheelite by reacting with $BrF_5$ (Clayton and Mayeda, 1963) and converted to $CO_2$ on a platinum-coated carbon rod. The $\delta^{18}O$ ratios were determined on a MAT-253 mass spectrometer. The reproducibility for isotopically homogeneous scheelite was about ±0.1‰ (1σ).

Carbon and oxygen isotope analyses of calcite were performed with the phosphoric acid method (Hoefs et al., 1987). The isotopic composition of $CO_2$ gas was measured by a MAT-253 mass spectrometer with a precision of ±0.2‰. Carbon isotope ratios were reported relative to the Peedee belemnite standard, and oxygen isotope ratios were reported relative to standard mean ocean water (SMOW). Oxygen and carbon isotopes were analyzed at the Stable Isotope Laboratory of Actlabs.

Individual sulfide minerals were carefully hand-picked under binocular microscopy after the ore samples were crushed, cleaned, and sieved to 40–60 meshes to obtain sulfide separates of >99% purity. Sulfur isotopes were analyzed using a Finnigan MAT-251EM mass spectrometer at the Stable Isotope Laboratory of Actlabs. The sulfur isotope values, with analytical precision of about ±0.2‰, were reported using the notation in per mil, relative to the Cañón Diablo troilite.

Lead isotope measurements were conducted on a Finnigan MAT-262 thermal ionization mass spectrometer at the Stable Isotope Laboratory of Actlabs. Approximately 50–60 mg powder for each sulfide sample and 150–200 mg powder for each whole-rock sample were weighed into 248 Teflon capsules and dissolved in distilled HF + $HNO_3$ at 150 °C for 7 days. Lead was separated on Teflon® columns containing about 100 μl AG1-X8, 100–200 mesh, by using an HBr–HCl wash and

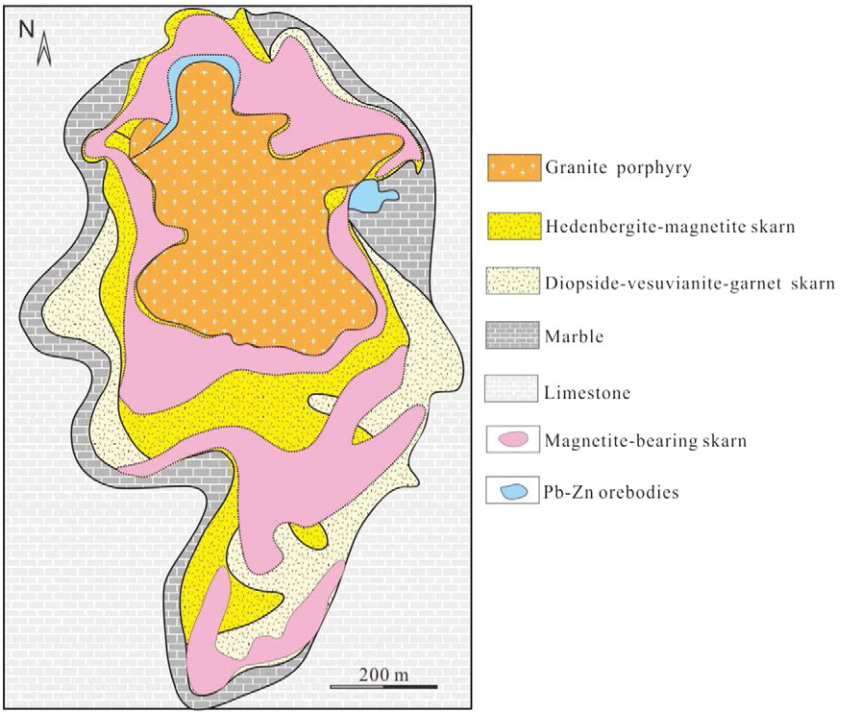


**Fig. 5.** Skarn zonation and mineralization at 273 m asl for the Huangshaping deposit.

elution procedure. Procedural blanks were <0.2 ng for Pb. Lead was loaded with a mixture of Si gel and $H_3PO_4$ onto a single Re filament and analyzed at 1300 °C. The measured lead isotope ratios were corrected for instrumental mass fractionation of 0.11% per atomic mass unit by references to repeated analyses of NBS-981 Pb standard.

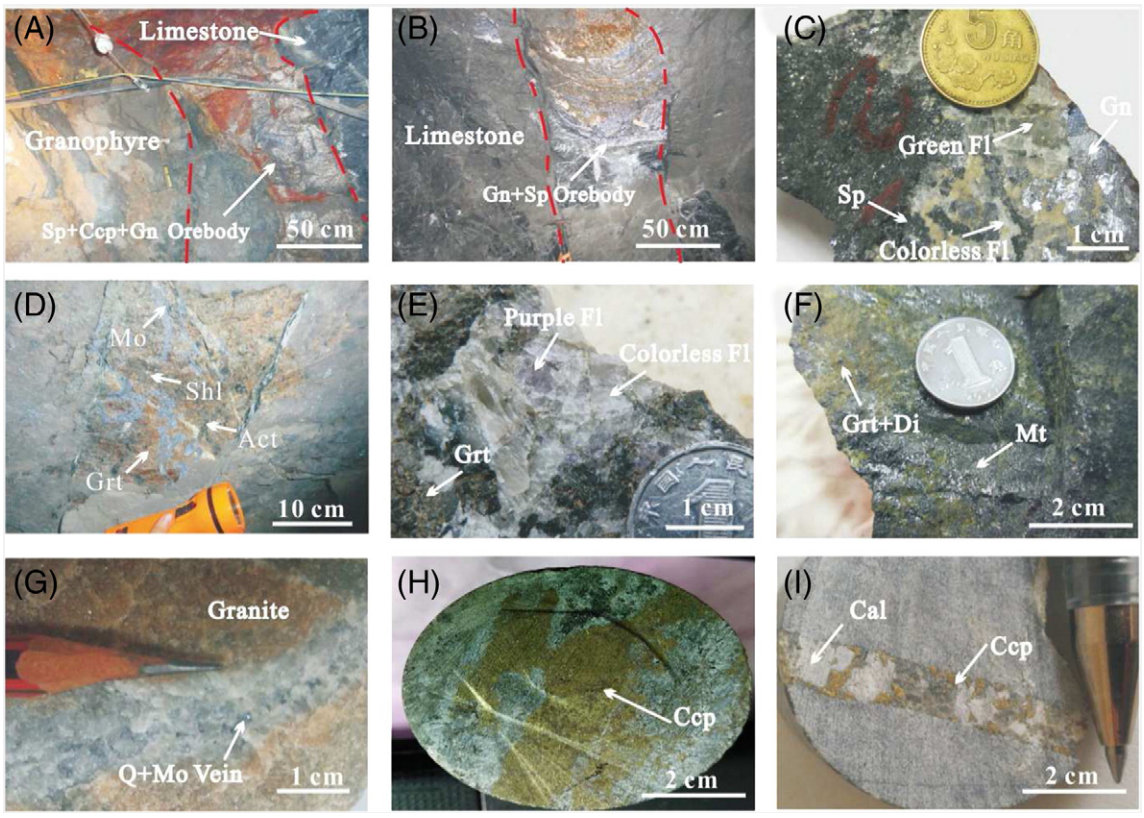


**Fig. 6.** Ore structures and relations for the Huangshaping deposit. (A) Pb–Zn ore and its relation to limestone and granophyre. (B) Pb–Zn orebody. (C) Pb–Zn ore. (D) W–Mo orebody in cluster No. 1. (E) Fluorite (purple and colorless) in garnet skarn. (F) Magnetite-bearing garnet diopside skarn. (G) Quartz–molybdenite vein in granite. (H) Massive chalcopyrite in skarn. (I) Chalcopyrite + scheelite + calcite vein in skarn. Abbreviations: Act = actinolite, Cal = calcite, Ccp = chalcopyrite, Di = diopside, Fl = fluorite, Gn = galena, Grt = garnet, Mo = molybdenite, Mt = magnetite, Po = pyrrhotite, Py = pyrite, Q = quartz, Shl = scheelite, Sp = sphalerite.

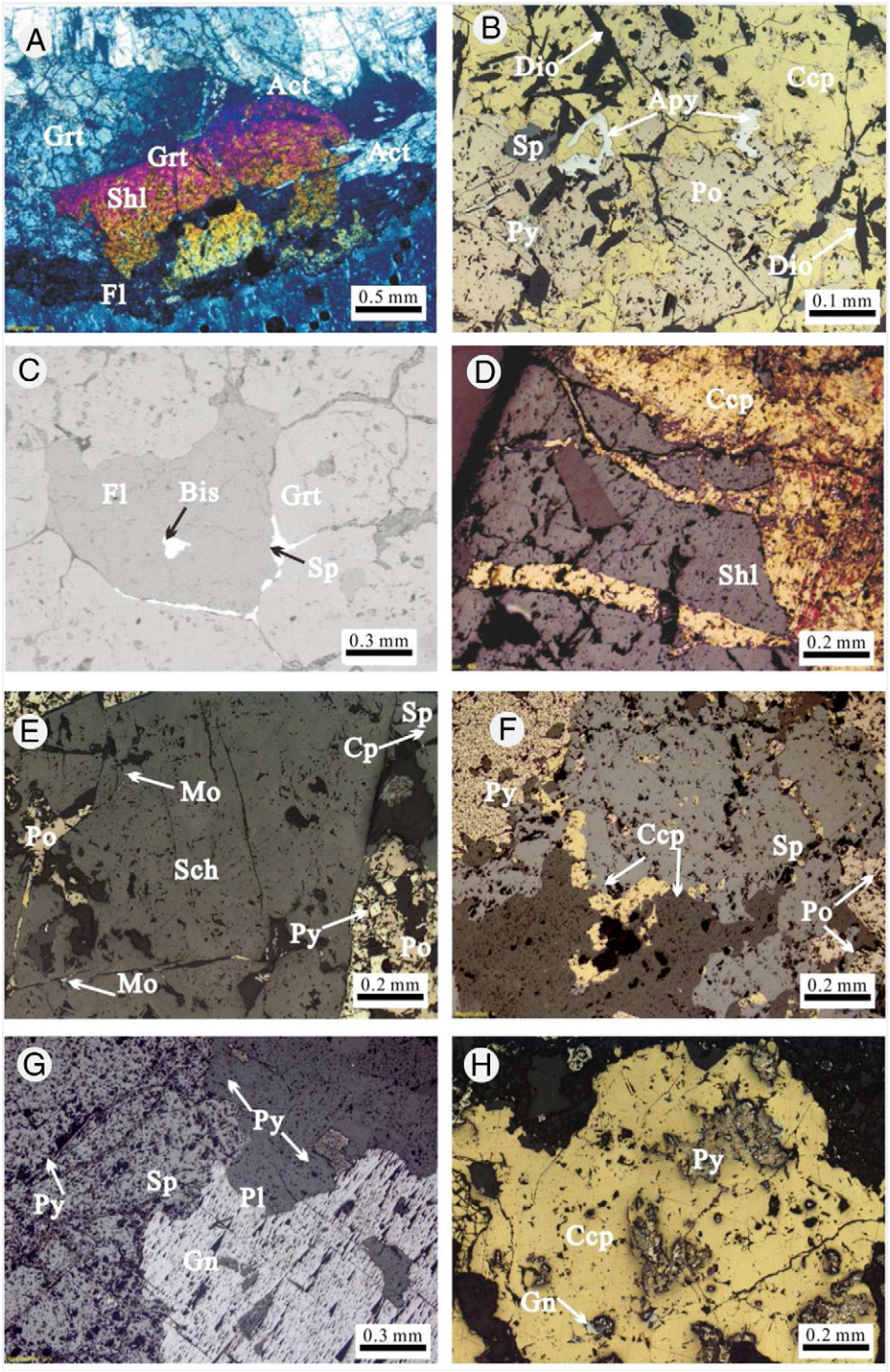


**Fig. 7.** Photomicrographs of ores from the Huangshaping deposit. (A) Scheelite truncated by fluorite veins in garnet–actinolite skarn. (B) Fine diopside within the ore. Chalcopyrite and pyrrhotite occur as fillings and replacement around arsenopyrite. Chalcopyrite replaces pyrrhotite. Sphalerite and chalcopyrite constitute a solid solution exsolution structure. (C) Backscattered electron image showing sphalerite with fluorite within garnet and bismuthinite as an inclusion within fluorite. (D) Chalcopyrite filling cracks within scheelite. (E) Pyrrhotite, molybdenite, sphalerite, and galena occurring as fillings within scheelite. Sphalerite and chalcopyrite show solid solution exsolution structure. (F) Pyrite, pyrrhotite, and sphalerite partially replaced by chalcopyrite in Pb–Zn ore. (G) Galena and sphalerite truncated by pyrite veins in Pb–Zn ore. (H) Hydrothermal breccia Cu ore. Abbreviations: Apy = arsenopyrite, Act = actinolite, Bis = bismuthinite, Ccp = chalcopyrite, Di = diopside, Fl = fluorite, Gn = galena, Grt = garnet, Mo = molybdenite, Mt = magnetite, Po = pyrrhotite, Py = pyrite, Q = quartz, Shl = scheelite, Sp = sphalerite.

### *4.5. Sm–Nd isotopes*

Sm–Nd isotopic analysis of scheelite, calcite, and fluorite were performed on a Triton-MC mass spectrometer at Actlabs. Each mineral powder was dissolved in a mixture of HF, $HNO_3$, and $HClO_4$. Before decomposition, each sample was totally spiked with a $^{149}Sm$–$^{146}Nd$ mixed solution, and REEs were separated using conventional cation exchange techniques. Sm and Nd concentrations were separated by extraction chromatography on HDEHP-covered Teflon® powder. The accuracy of the measurements was ±0.5% for Sm and Nd contents and ±0.5% (2σ) for $^{147}Sm/^{144}Nd$.

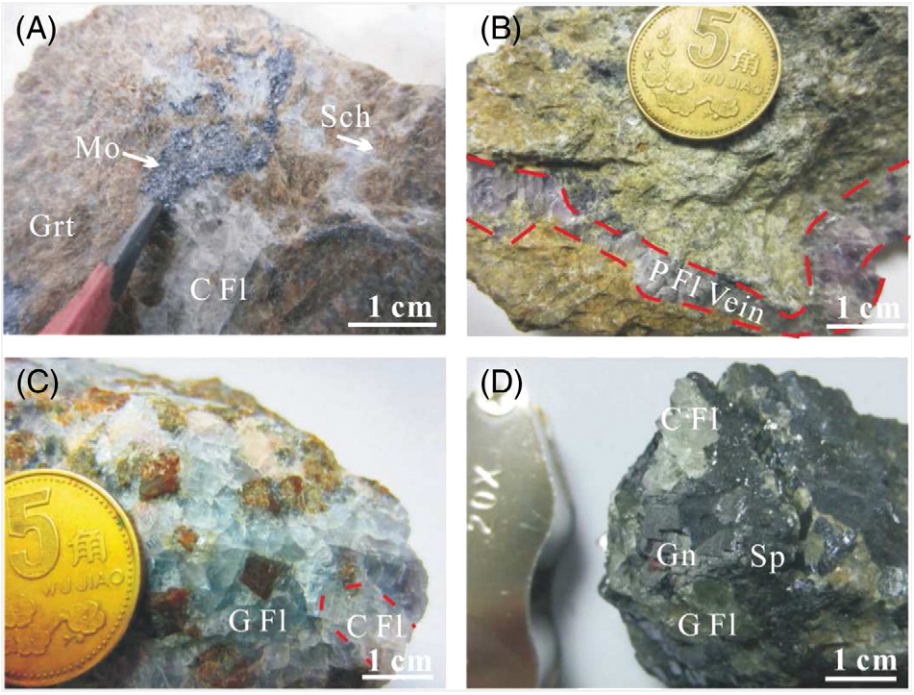


**Fig. 8.** Photographs showing occurrences of fluorite and calcite in W–Mo and Pb–Zn ores from the Huangshaping deposit. (A) Colorless fluorite veins with disseminated molybdenite and scheelite in garnet skarn. (B) Purple fluorite vein in actinolite skarn. (C) Green fluorite and colorless fluorite in W–Mo-bearing garnet skarn. (D) Assemblage of galena + sphalerite with green fluorite and colorless fluorite in Pb–Zn ore. Abbreviations: C Fl = colorless fluorite, G Fl = green fluorite, Gn = galena, Grt = garnet, Mo = molybdenite, P Fl = purple fluorite, Sch = scheelite, Sp = sphalerite.

## 5. Results

### 5.1. Fluid inclusions

#### 5.1.1. Fluid inclusion petrography

According to the criteria of Roedder (1984), fluid inclusions are classified as primary, secondary, or pseudosecondary. Fluid inclusions for microthermometric analysis were selected to represent discrete groups of inclusions with constant liquid/vapor/solid ratios and coherent homogenization temperatures and without post-entrapment re-equilibration or leakage.

Three types of fluid inclusions were observed in samples from the Huangshaping deposit (Table 3; Fig. 9):

Type I inclusions are aqueous liquid–vapor ones, which are further divided into Type Ia (Fig. 9A) and Type Ib (Fig. 9B) in terms of mode of homogenization and relative volume of vapor–liquid phases. Type Ia aqueous inclusions are liquid rich (vapor < 40% by volume) and homogenized into a liquid phase. Type Ib is vapor rich (vapor > 40% by volume) that homogenizes into a vapor phase.

Type II aqueous inclusions are daughter-mineral-bearing inclusions. They are subdivided into Type IIa (Fig. 9C–E) and Type IIb (Fig. 9F). When heated, halite in Type IIa inclusions dissolves before the vapor

**Table 3**
Types of fluid inclusions in garnet, molybdoscheelite, quartz, calcite, fluorite, scheelite, and actinolite from W-Mo skarns, Pb-Zn veins, Mo-bearing quartz veins, and Cu-bearing calcite veins at the Huangshaping Deposit.

| Sample | Mineral[1] | Fl type | V (vol%) | Homogenization T (°C) | Salinity (wt% NaCl eqv.) |
|---|---|---|---|---|---|
| Skarn | Garnet (6) | Type Ia | 16–30 | To liquid: >600 | |
| | Garnet (3) | Type Ib | 66–85 | To vapor: 584 → 600 | 3–5 |
| | Garnet (38) | Type IIa | 9–33 | Vapor: 530 → 600; halite: 323–346 | 40–42 |
| | Actinolite (10) | Type IIa | 25–40 | Vapor: 568 → 600; halite: 357–381 | 43–45 |
| | Molybdoscheelite (39) | Type IIa | 10–33 | Vapor: 381–488; halite: 306–372 | 39–45 |
| | Molybdoscheelite (8) | Type Ia | 20–30 | | 8–9 |
| Skarn W-Mo | Calcite (24) | Type Ia | 14–25 | To liquid: 286–405 | 15–22 |
| | Purple fluorite (7) | Type IIb | 7–35 | Vapor: 200–310; halite: 250–303 | 35–41 |
| | Purple fluorite (38) | Type Ia | 5–22 | To liquid: 202–354, Tm = 1–6.5 | 9–16 |
| | Colorless fluorite (116) | Type Ia | 8–40 | To liquid: 220–380, Tm = 0.1–0.6 | 6–13 |
| | Green fluorite (12) | Type Ia | 7–38 | To liquid: 230–303, Tm = 0.1 | 8–15 |
| | Quartz (22) | Type Ia | 15–40 | To liquid: 300–367 | 7–16 |
| Mo-bearing quartz veins | Quartz (7) | Type Ib | 55–70 | To vapor: 316–435 | 13–17 |
| | Quartz (2) | Type III | 20–35 | To vapor: 237, Tm = 5.1 | 8–9 |
| Pb-Zn veins | Green fluorite (42) | Type Ia | 10–40 | To liquid: 170–313, Tm = 1.1–4.5 (21) | 2–16 |
| | Colorless fluorite (116) | Type Ia | 7–30 | To liquid: 165–306, Tm = 0.2–3 (6) | 5–15 |
| | Scheelite (14) | Type IIa | 10–30 | Vapor: 463–517; halite: 250–271 | 35–36 |
| Chalcopyrite-calcite veins | | Type Ia | 6–20 | To liquid: 366–485 | 8.4–9.3 |
| | Calcite (26) | Type Ia | 8–30 | To liquid: 172–275 | 5–19 |

Abbreviations: Type Ia: liquid-rich aqueous inclusions; Type Ib: vapor-rich aqueous inclusions; Type IIa: daughter mineral-bearing aqueous inclusions, homogenized by the vapor disappearance; Type IIb: daughter mineral-bearing aqueous inclusions, homogenized by the daughter-mineral disappearance; Type III:$CO_2$-bearing inclusions. [1]Number in parentheses = number of measurements.

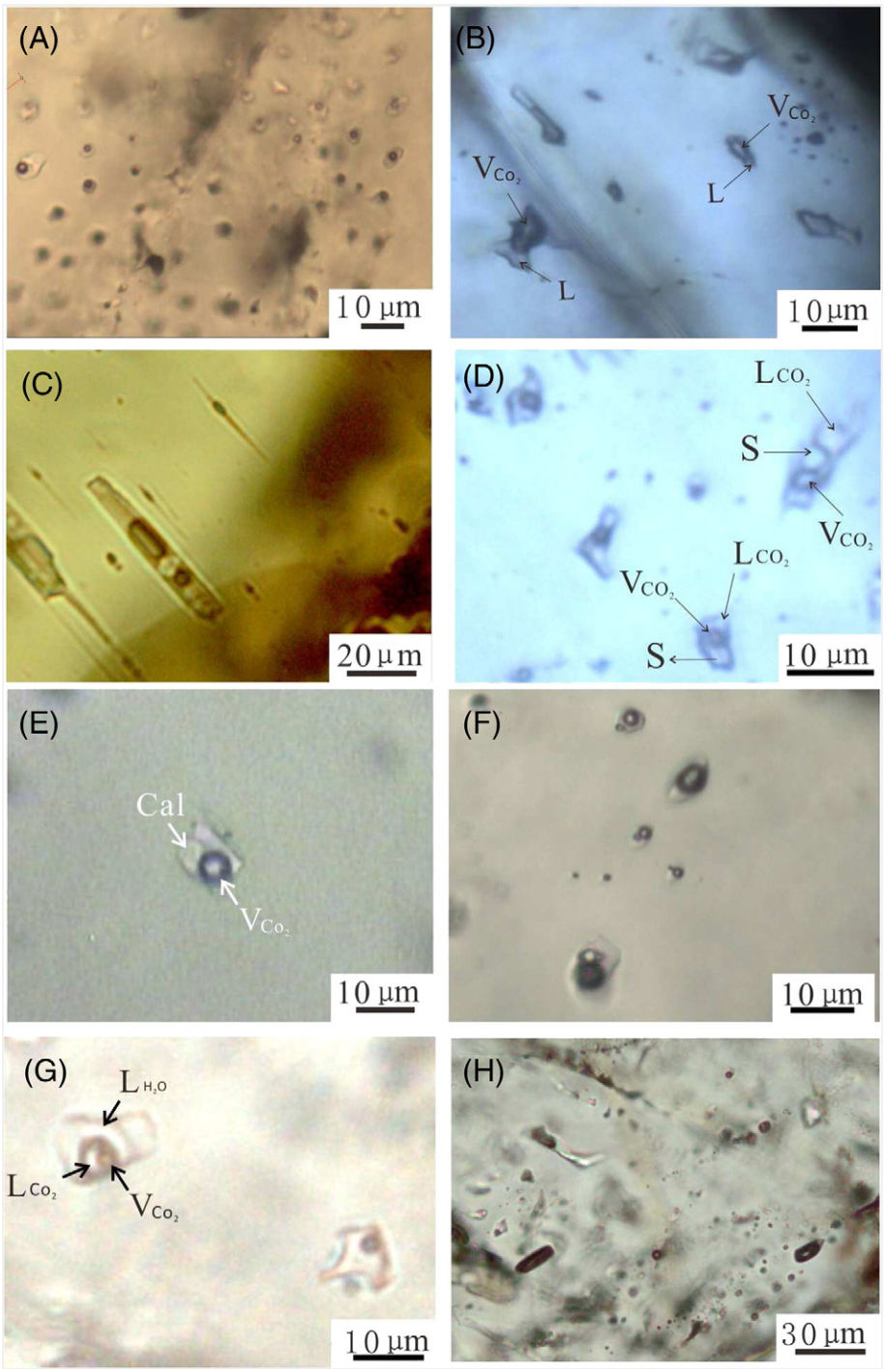


**Fig. 9.** Photomicrographs showing types of fluid inclusions from various ores from the Huangshaping deposit. (A) Low-salinity Type Ia inclusions within green fluorite. (B) Type Ib fluid inclusions within garnet. (C) Type IIa multi-solid fluid inclusions within actinolite. (D) Type IIa fluid inclusions within garnet. (E) Type Ia calcite-bearing daughter crystal fluid inclusion within purple fluorite. (F) Type IIb fluid inclusions within purple fluorite. (G) Coexisting Type III and Type Ia inclusions within purple fluorite. (H) Coexisting vapor-rich and liquid-rich inclusions within quartz. Abbreviations: Cal = calcite, H = halite, $L_{CO2}$ = liquid $CO_2$, $L_{H2O}$ = liquid water, S = unknown solid mineral, $V_{CO2}$ = vapor $CO_2$.

disappearance. For inclusions of Type IIb, halite dissolution precedes vapor disappearance upon heating. Daughter mineral crystals within Type II inclusions are either transparent or opaque and include NaCl, KCl, and $CaCO_3$.

Type III inclusions are $CO_2$-bearing aqueous inclusions (Fig. 9G). $CO_2$ is determined either direct as a liquid rim on the vapor phase or more commonly via decomposition of $H_2O$–$CO_2$ clathrate during the thawing cycle.

*5.1.2. Fluid inclusion microthermometry and salinity*

A total of 530 fluid inclusions were selected for microthermometrical measurement. The salinities of the inclusions are reported as wt% NaCl equiv. Detailed microthermometry data are listed in Table 3 and shown in Figs. 10 and 11.

*5.1.2.1. Skarn minerals.* Fluid inclusions in garnet are mainly Type Ib and Type IIa inclusions that coexist in the same garnet grain. Type IIa

inclusions homogenized by vapor disappearance at 528 °C to >600 °C after halite dissolution at 323 °C–353 °C. The salinities of Type IIa inclusions range from 40 to 43 wt% NaCl equiv. Type Ib inclusions do not homogenize after being heated up to 600 °C, and their salinities range from 3.1 to 4.7 wt% NaCl equiv. Fluid inclusions in actinolite are mainly of Type IIa and they homogenized by vapor disappearance (>600 °C)

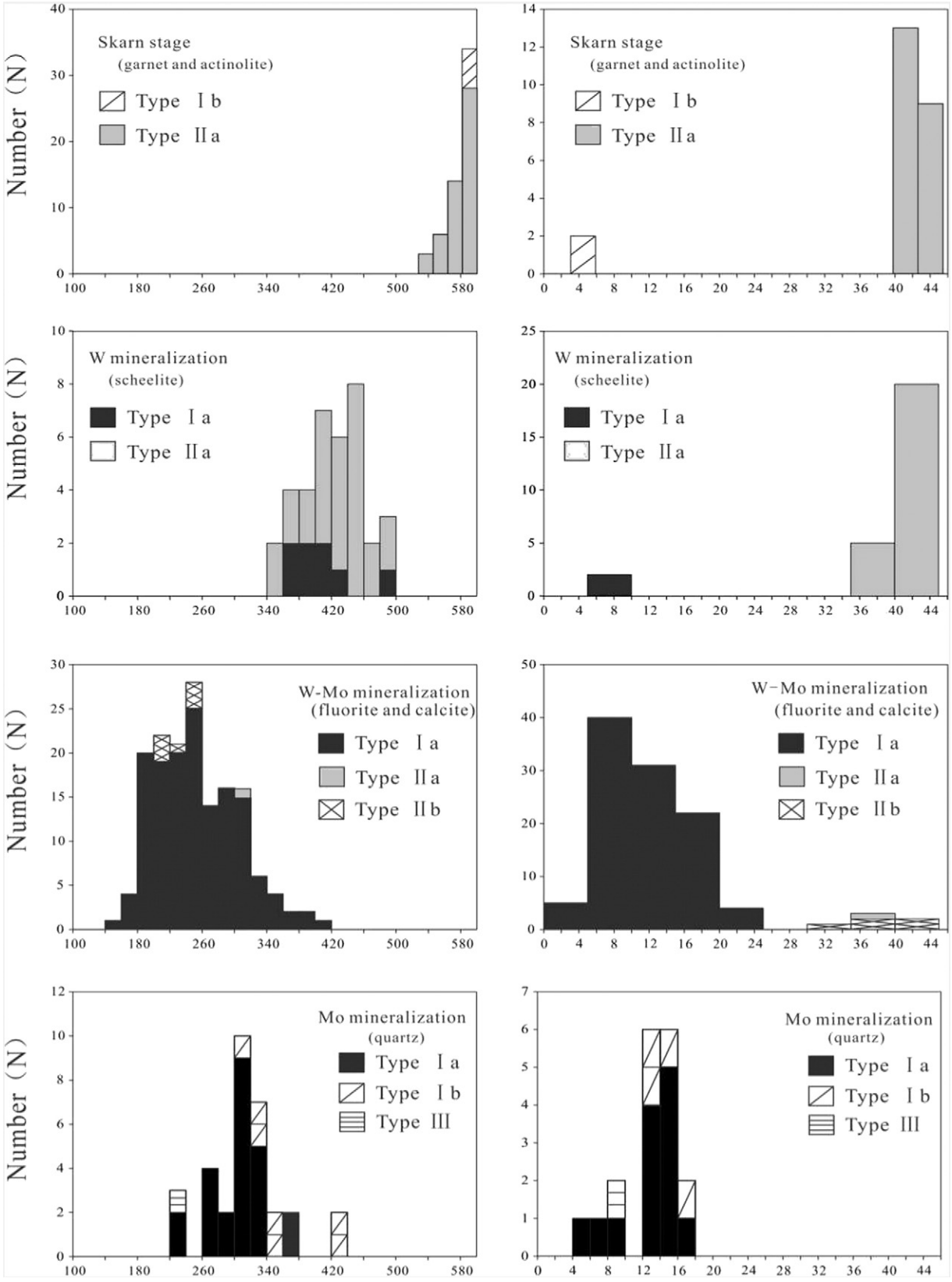


**Fig. 10.** Diagrams showing statistics for homogenization temperature and salinity of fluid inclusions obtained from different minerals collected from skarn and different types of ores from the Huangshaping deposit. Left panels: Histograms of cumulative frequency of homogenization temperature. Right panels: Histograms of salinities for three types of fluid inclusions.

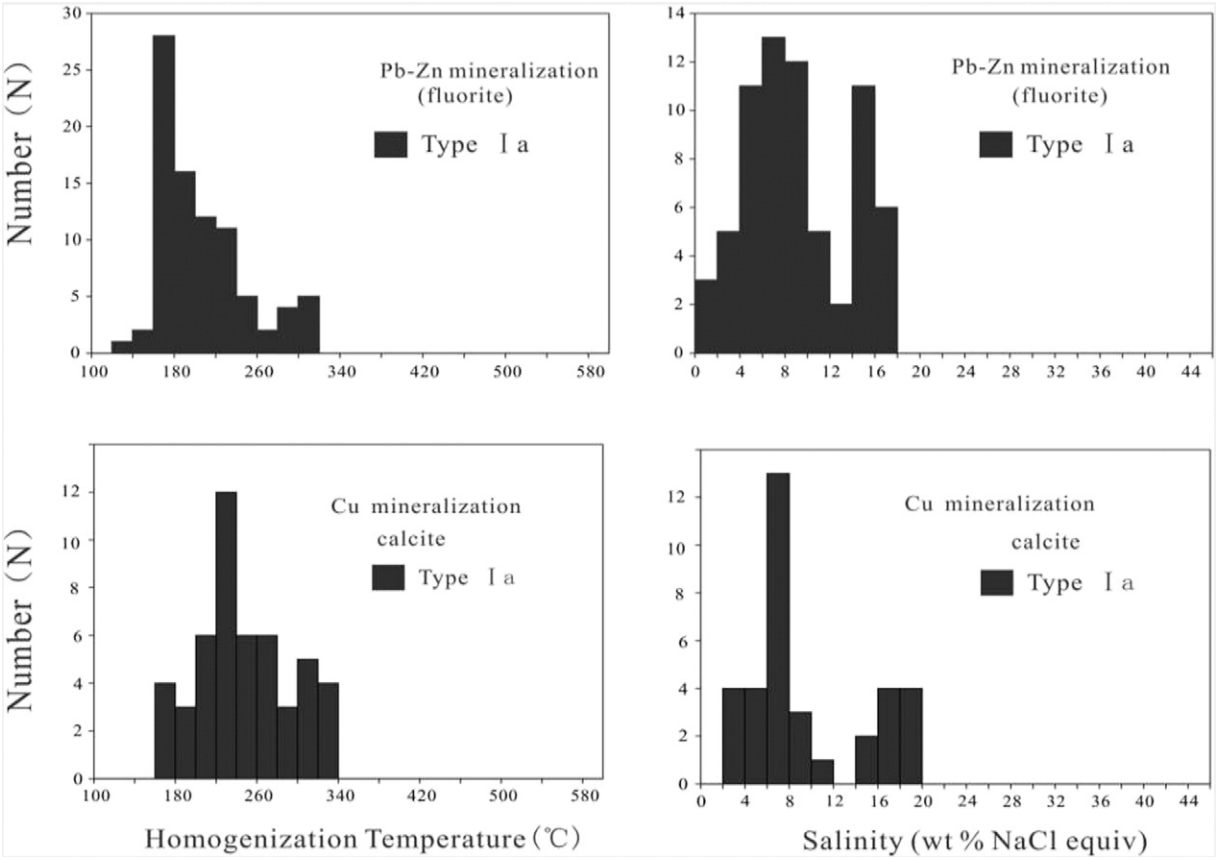


**Fig. 10** (*continued*).

after halite dissolution (357 °C–381 °C); their salinities range from 43 to 46 wt% NaCl equiv.

*5.1.2.2. W–Mo ores.* Fluid inclusions in molybdoscheelite with yellow luminescence in skarns contain abundant Type IIa and Type Ib inclusions with a minor amount of Type Ia inclusions. Type IIa inclusions contain multi-solid phases that homogenized by vapor disappearance (347 °C–488 °C) after halite dissolution (288 °C–372 °C); their salinities range from 37 to 45 wt% NaCl equiv. Type Ia inclusions exhibit final ice melting temperatures at −5.4 °C to −6.1 °C, indicating that their salinities range from 8.4 to 9.3 wt% NaCl equiv. This type of inclusion homogenized to a liquid phase at temperatures between 367 °C and 485 °C.

Fluid inclusions in fluorite (purple, colorless, and green) and calcite related to W–Mo ores are composed of Type Ia, Type IIa, Type IIb, and Type III inclusions.

In purple fluorite, Type Ia inclusions homogenized to liquid at 175 °C–310 °C and exhibit final ice melting temperatures from −15.6 °C to −3.1 °C, indicating salinities ranging from 5.1 to 19.1 wt%

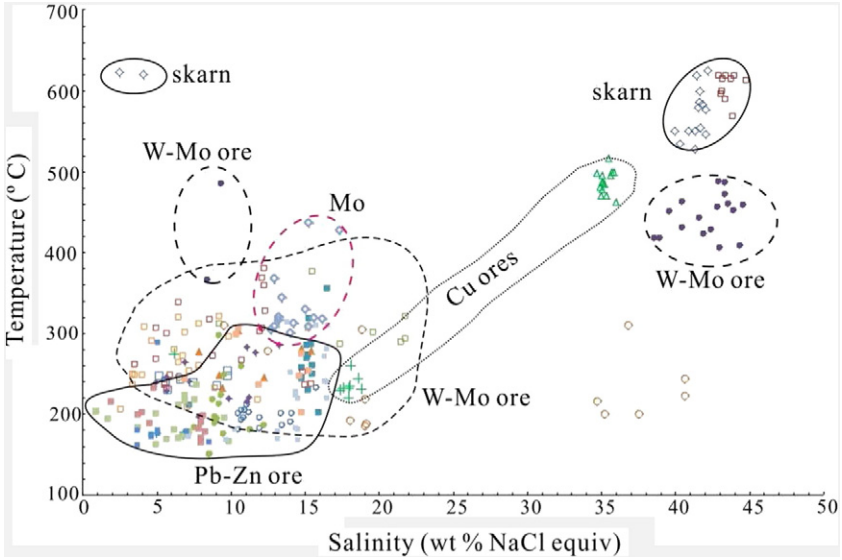


**Fig. 11.** Plots of homogenization temperature vs. salinity of fluid inclusions.

**Table 4**
Trace element concentrations in fluorite from ores at the Huangshaping Deposit, South China.

| Samples | W-Mo | | | | | | | | Pb-Zn | | | | Cu | |
|---|---|---|---|---|---|---|---|---|---|---|---|---|---|---|
| | HSP-84–1 | HSP-84–2 | HSP-84-3 | HSP-28-0 | HSP-28-2 | HSP-28-3 | HSP-135-2 | HSP-247-2 | HSP-33-2 | HSP-33-3 | HSP-107-2 | HSP-107-3 | HSP-211-1 | HSP-211-3 |
| Na (%) | 0.09 | 0.06 | 0.04 | 0.05 | 0.05 | 0.05 | 0.05 | 0.04 | 0.09 | 0.09 | 0.09 | 0.08 | 0.05 | 0.06 |
| Mg (%) | 0.01 | 0.01 | 0.01 | 0.01 | <0.01 | 0.01 | <0.01 | <0.01 | <0.01 | 0.01 | 0.03 | 0.01 | 0.01 | <0.01 |
| Al (%) | 0.17 | 0.13 | 0.08 | 0.02 | 0.01 | 0.09 | 0.05 | 0.06 | 0.02 | 0.09 | 0.16 | 0.05 | 0.14 | 0.1 |
| K (%) | 0.13 | 0.12 | 0.1 | 0.11 | 0.11 | 0.1 | 0.09 | 0.1 | 0.1 | 0.13 | 0.12 | 0.11 | 0.12 | 0.11 |
| Ca (%) | >50.0 | >50.0 | >50.0 | 35.8 | 33.8 | 48 | 42.3 | 43.7 | 42.4 | 40.1 | 49.7 | 43.5 | 45.9 | 46.5 |
| Fe (%) | 0.13 | 0.13 | 0.13 | 0.09 | 0.09 | 0.16 | 0.13 | 0.14 | 0.11 | 0.1 | 0.25 | 0.12 | 0.19 | 0.13 |
| ($\times 10^{-6}$) | | | | | | | | | | | | | | |
| Li | 1.4 | 1 | 0.6 | <0.5 | 0.6 | 1.1 | 0.5 | 0.7 | <0.5 | 0.7 | 1.3 | 0.5 | 1 | 0.6 |
| Cr | 17.5 | 3.4 | 1.8 | 5.1 | 18.6 | 9.3 | <0.5 | 3 | 3.3 | 3.4 | 10.5 | 5.9 | 7.1 | 3.9 |
| Mn | 42 | 31 | 25 | 23 | 28 | 104 | 74 | 47 | 51 | 6 | 808 | 26 | 282 | 19 |
| Ni | 14.9 | 17 | 18.7 | 15.6 | 14.3 | 21.3 | 21 | 21.6 | 18.1 | 16.4 | 18.3 | 16.8 | 20.3 | 22 |
| Co | 0.8 | 0.8 | 0.9 | 0.7 | 0.6 | 0.9 | 0.9 | 0.9 | 0.8 | 0.9 | 0.9 | 0.8 | 0.9 | 1.1 |
| Bi | 130 | 9.34 | 0.81 | 16.1 | 18.6 | 9.13 | 0.44 | 0.84 | 0.37 | 0.26 | 86.4 | 1.63 | 7.36 | 8.7 |
| Se | <0.1 | 0.5 | 0.2 | <0.1 | <0.1 | <0.1 | <0.1 | <0.1 | <0.1 | <0.1 | 2.8 | 0.7 | <0.1 | <0.1 |
| Zn | 15.9 | 7.4 | 31.8 | 9.3 | 5.3 | 25.5 | 37.5 | 12.3 | 6.6 | 21.1 | 53.7 | 19.9 | 23.1 | 7.6 |
| As | 5.6 | 3.9&& | 19.3 | 0.3 | <0.1 | 1.6 | <0.1 | 1 | <0.1 | 18.1 | 68.1 | 3.3 | 2.7 | 20.1 |
| Rb | 1.3 | 1 | 0.5 | 0.7 | 0.8 | 1.6 | 0.9 | 0.8 | 0.5 | 1 | 1.4 | 0.8 | 2.7 | 1.1 |
| Y | 9.2 | 17.6 | 54.7 | 1.2 | 0.9 | 56.1 | 2.6 | 0.3 | 0.5 | 1.7 | 259 | 55.2 | 13.5 | 111 |
| Sr | 13.9 | 12.5 | 50.4 | 13.4 | 12.6 | 15.3 | 22.9 | 17.4 | 6 | 7.6 | 19.1 | 6.3 | 16.2 | 9 |
| Nb | 17.6 | 8.9 | 6.3 | 2.8 | 2.2 | 3.0 | 1.7 | 1.7 | 2.6 | 2.7 | 5.0 | 3.4 | 3.1 | 1.8 |
| Mo | 0.4 | <0.1 | 0.9 | 0.7 | <0.1 | 0.8 | 4.8 | 4.3 | <0.1 | <0.1 | 0.3 | <0.1 | 38.1 | 0.7 |
| Cu | 3 | 2.2 | 6.1 | 1.9 | 1.6 | 4.2 | 2.2 | 1 | 2.2 | 1.5 | 9 | 2.4 | 8.8 | 8.8 |
| Sb | <0.1 | <0.1 | <0.1 | <0.1 | 0.1 | <0.1 | <0.1 | <0.1 | <0.1 | <0.1 | 0.4 | 0.1 | 0.3 | <0.1 |
| Te | 1.1 | 0.3 | 0.4 | 0.6 | 0.8 | 0.5 | 0.4 | 0.3 | 0.6 | 0.2 | 0.4 | 0.3 | 1.3 | 1.1 |
| La | 0.69 | 0.56 | 27.7 | 0.76 | 0.62 | 2.93 | 0.72 | 0.22 | 0.71 | 5.87 | 13.1 | 34.6 | 9.05 | 18.1 |
| Ce | 1.3 | 1.11 | 54.9 | 1.12 | 0.97 | 3.76 | 1.41 | 0.48 | 1.14 | 10.3 | 26.5 | 75 | 18.6 | 40.1 |
| Pr | 0.16 | 0.13 | 6.77 | 0.12 | 0.12 | 0.34 | 0.17 | 0.05 | 0.14 | 1.27 | 3.85 | 11.3 | 1.67 | 5.91 |
| Nd | 0.72 | 0.63 | 29 | 0.59 | 0.56 | 1.47 | 0.62 | 0.14 | 0.62 | 5.75 | 21.7 | 59.1 | 5.26 | 31.4 |
| Sm | 0.26 | 0.17 | 9.03 | 0.27 | 0.2 | 0.49 | 0.11 | <0.01 | 0.1 | 0.91 | 9.19 | 15 | 1.2 | 7.77 |
| Eu | 0.018 | 0.006 | 1.23 | 0.006 | 0.014 | 0.005 | 0.012 | <0.005 | 0.018 | 0.089 | 0.093 | 0.09 | 0.035 | 0.03 |
| Gd | 0.28 | 0.43 | 7.92 | 0.6 | 0.57 | 0.92 | 0.16 | <0.01 | 0.18 | 0.88 | 15.5 | 14.8 | 1.18 | 9.35 |
| Tb | 0.06 | 0.09 | 1.32 | 0.15 | 0.15 | 0.21 | 0.03 | <0.01 | 0.03 | 0.11 | 2.63 | 1.81 | 0.22 | 1.12 |
| Dy | 0.51 | 0.66 | 6.61 | 1.16 | 1.16 | 1.6 | 0.14 | 0.02 | 0.18 | 0.49 | 15.2 | 8.86 | 1.32 | 5.85 |
| Ho | 0.12 | 0.15 | 1.12 | 0.26 | 0.26 | 0.39 | 0.02 | <0.01 | 0.04 | 0.08 | 2.65 | 1.66 | 0.25 | 1.04 |
| Er | 0.36 | 0.45 | 2.48 | 0.74 | 0.75 | 1.22 | 0.06 | 0.02 | 0.13 | 0.18 | 5.38 | 4.35 | 0.67 | 2.55 |
| Tm | <0.005 | <0.005 | 0.275 | 0.096 | 0.096 | 0.157 | <0.005 | <0.005 | <0.005 | <0.005 | 0.39 | 0.52 | 0.091 | 0.303 |
| Yb | 0.38 | 0.27 | 1.38 | 0.54 | 0.53 | 0.86 | 0.07 | 0.02 | 0.09 | 0.1 | 1.1 | 2.74 | 0.55 | 1.61 |
| Lu | 0.049 | 0.038 | 0.17 | 0.059 | 0.059 | 0.088 | 0.01 | 0.004 | 0.015 | 0.012 | 0.066 | 0.356 | 0.087 | 0.196 |
| W | 17.5 | 42.4 | 1.7 | 3.7 | 4.6 | 9.6 | 30.7 | 20.8 | <0.1 | <0.1 | 12.2 | 0.4 | 8.1 | 1.8 |
| Pb | 4.4 | 6.4 | 3.5 | 2.1 | 2.3 | 2.9 | 2.1 | 2.2 | 44.1 | 16.6 | 16.4 | 23.4 | 2.8 | 1.4 |
| Th | 1.6 | 0.9 | 0.9 | 1 | 0.9 | 0.2 | 0.1 | 0.2 | 1.1 | 0.9 | 1.2 | 1.4 | 0.4 | 0.2 |
| U | 0.07 | 0.08 | 0.06 | 0.06 | 0.07 | 0.33 | 0.19 | 0.06 | 0.04 | 0.04 | 0.17 | 0.05 | 2.8 | 0.31 |
| Th | 0.37 | 0.25 | 0.19 | 0.1 | 0.09 | 0.15 | 0.08 | 0.14 | 1.15 | 1.76 | 0.19 | 0.19 | 1.01 | 0.12 |
| Y/Ho | 72.5 | 104.0 | 45.2 | 133.5 | 128.1 | 125.4 | 125 | – | 162.5 | 158.8 | 95.1 | 131.3 | 46.8 | 95.3 |
| Tb/La | 0.09 | 0.16 | 0.05 | 0.20 | 0.24 | 0.07 | 0.04 | – | 0.04 | 0.02 | 0.05 | 0.04 | 0.02 | 0.06 |
| Ce/Yb | 3.42 | 4.11 | 39.78 | 2.07 | 1.83 | 4.37 | 20.14 | 24.00 | 12.67 | 103.00 | 24.09 | 27.37 | 33.82 | 24.91 |
| Sr/Y | 1.51 | 0.71 | 0.92 | 11.70 | 14.00 | 0.27 | 8.81 | 58.00 | 12.00 | 4.47 | 0.07 | 0.11 | 1.20 | 0.08 |
| ΣREE | 13.61 | 20.29 | 200.51 | 41.17 | 39.36 | 63.34 | 6.03 | 0.95 | 9.89 | 38.74 | 369.35 | 448.19 | 51.88 | 244.43 |
| δEu | 0.20 | 0.07 | 0.44 | 0.05 | 0.13 | 0.02 | 0.25 | – | 0.41 | 0.30 | 0.02 | 0.02 | 0.09 | 0.11 |
| δCe | 0.94 | 0.99 | 0.96 | 0.89 | 0.85 | 0.90 | 0.97 | 1.10 | 0.87 | 0.90 | 0.89 | 0.91 | 1.15 | 0.93 |

NaCl equiv. Type IIa inclusions homogenized by vapor disappearance (310 °C) after halite dissolution (282 °C); their salinity is 37–40 wt% NaCl equiv. Type IIb inclusions homogenized by halite dissolution (250 °C–303 °C) after vapor disappearance (200 °C–252 °C); their salinity ranges from 35 to 41 wt% NaCl equiv. Type III inclusions exhibit final melting temperatures of clathrates ($T_m$ = −1 °C to 6.5 °C), indicating a salinity range of 6.5–16.5 wt% NaCl equiv, and they homogenized to vapor from 229 °C to 355 °C. Laser Raman spectroscopy showed that vapor-rich inclusions in purple fluorite were occasionally composed of $H_2O + CO_2$, and their daughter minerals were calcite (Fig. 9E) and halite, indicating oversaturation of $CO_2$ in fluids.

Type Ia inclusions in green fluorite exhibit final ice melting temperatures at −10.8 °C to −5.0 °C, indicating that their salinities range from 7.9 to 11.8 wt% NaCl equiv. This type of inclusion homogenized to liquid at temperatures between 160 °C and 303 °C. Type III inclusions in green fluorite exhibit a final melting temperature of clathrates ($T_m$ = 0.1°), indicating that their salinity is 15.4 wt% NaCl equiv. These inclusions homogenized to vapor at 279 °C. Type Ia inclusions in colorless fluorite exhibit final ice melting points at −11.8 °C to −2.1 °C, indicating that their salinities range from 3.6 to 15.8 wt% NaCl equiv. This type of inclusion homogenized to liquid at temperatures between 150 °C and 381 °C. Type III inclusions in colorless fluorite exhibit final melting temperatures of clathrates ($T_m$ = 0.1 °C to 0.6 °C), indicating a salinity range of 14.9 to 15.4 wt% NaCl equiv. They homogenized to vapor at 236 °C–252 °C. Fluid inclusions in calcite in W–Mo ores are mainly Type Ia inclusions. They exhibit final ice melting temperature at −21.6 °C to −11.5 °C, indicating that their salinities range from 15.0 to 23.2 wt% NaCl equiv. This type of inclusion homogenized to liquid at temperature between 284 °C and 405 °C.

Type IIb inclusions that homogenized by halite dissolution are also reported in other hydrothermal deposits (e.g., Bodnar, 1995). This type of fluid inclusion can be generated either through direct exsolution from parent magmas (e.g., Cline and Bodnar, 1994) or through a process of post-entrapment modification (e.g., Klemm et al., 2008), or else trapped after undergoing overpressuring (e.g., Baker and Lang, 2003). In the Huangshaping deposit, the Type IIb fluid inclusions in purple fluorite with W–Mo ore show a coexistent relationship with the Type Ia fluid inclusions, suggesting that they were generated from post-entrapment modification of brine inclusions homogenized through vapor disappearance resulting from loss of $H_2O$ (Audétat and Günther, 1999).

Fluid inclusions in quartz grains sampled from quartz + molybdenite veins include Type Ia, Type Ib, and Type III inclusions (Fig. 9H). Type Ia inclusions in the quartz exhibit final ice melting temperatures at −12.3 °C to −3.6 °C, indicating salinities of 5.9 to 16.2 wt% NaCl equiv. These inclusions homogenized to liquid at temperatures between 228 °C and 372 °C. Type Ib inclusions exhibit final ice melting temperatures at −13.5 °C to −9.4 °C, indicating that their salinities range from 13.3 to 17.3 wt% NaCl equiv. These inclusions homogenized to liquid at temperatures between 316 °C and 435 °C. Type III inclusions in quartz exhibit a final melting temperature of clathrates ($T_m$ = 5.1 °C), indicating a salinity of 8.8 wt% NaCl equiv. These inclusions homogenized to vapor at 236 °C. Laser Raman spectroscopy shows that vapor-rich inclusions in quartz were occasionally composed of $CO_2 + CH_4$.

*5.1.2.3. Pb–Zn ores.* Fluid inclusions in green and colorless fluorite in Pb–Zn ores are mainly Type Ia, Type Ib, and Type III inclusions. In green fluorite, fluid inclusions present as Type Ia and Type III. Type Ia inclusions exhibit final ice melting temperatures at −1.1 °C to −5.3 °C, indicating salinities of 1.9–8.3 wt% NaCl equiv. These inclusions homogenized to liquid at temperatures between 135 °C and 235 °C. Type III inclusions exhibit final melting temperatures of clathrates ($T_m$ = −1.1 °C to 4.5 °C), indicating salinities ranging between 9.7 and 16.5 wt% NaCl equiv. These inclusions homogenized to vapor at 167 °C to 313 °C. In

**Table 5**
Trace element concentrations in calcite from ores at the Huangshaping Deposit, South China.

| Samples | Ores | (%) | Na | Sr | Y/Ho | Mg | Al | K | Ca | Fe | ($\times 10^{-6}$) | La | Ce | Pr | Nd | Sm | Eu | Gd | Tb | Dy | Ho | Er | Tm | Yb | Lu | Y | Zr | Nb | Mo | Sb | Ba | Cd | V | Cr | Mn | Li | Ni | Cu | Be | Ag | Cs | Co | Eu | Bi | Zn | Ga | As |
|---|---|---|---|---|---|---|---|---|---|---|---|---|---|---|---|---|---|---|---|---|---|---|---|---|---|---|---|---|---|---|---|---|---|---|---|---|---|---|---|---|---|---|---|---|---|
| HSP-32-4 | W-Mo | | 0.08 | 248 | 34.0 | 0.24 | 0.45 | 0.15 | 38.9 | 1.2 | | 3.7 | 6.8 | 0.8 | 2.9 | 0.5 | 0.5 | 0.5 | <0.1 | 0.5 | 0.2 | 0.3 | <0.1 | 0.2 | <0.1 | 3.4 | 5 | 1.2 | 1.5 | 1 | 27 | 1.2 | 9 | 17.9 | >10.000 | 2.7 | 17.2 | 8.5 | <0.1 | 0.47 | 0.38 | 1.1 | 0.12 | 0.06 | 223 | 0.9 | 2 |
| HSP-84 | Pb-Zn | | 0.08 | 178 | 33.0 | 0.05 | 0.23 | 0.07 | 43.3 | 0.2 | | 9.2 | 21.3 | 2.4 | 7.3 | 1.5 | 1.2 | 0.2 | 0.2 | 0.7 | 0.7 | 8 | <0.1 | 0.2 | <0.1 | 3.3 | <1 | 0.3 | 0.9 | <0.1 | 6 | 0.2 | 3 | 10.1 | >10.000 | 1.2 | 17.4 | 0.1 | <0.1 | 0.06 | 0.08 | 0.8 | 0.22 | 0.13 | 26.5 | 0.4 | 1.9 |
| HSP-148 | Cu | | 0.17 | 57.9 | 32.9 | 0.06 | 0.32 | 0.14 | 46.4 | 0.28 | | 2.9 | 7.2 | 1.1 | 5.4 | 2.7 | 7.1 | 7.1 | 1.8 | 15.5 | 9.1 | 68.5 | <0.1 | 0.1 | 10.1 | 135 | <1 | <0.1 | 1.1 | 0.1 | 4 | <0.1 | 3 | 17.5 | 714 | 1.6 | 19 | 13.7 | 0.1 | 4.1 | 0.05 | 0.08 | 0.08 | 1.96 | 32.7 | 0.7 | 29.7 |
| HSP12–10 | Cu | | 0.19 | 59.2 | 25.1 | 0.16 | 0.46 | 0.39 | >50.0 | 0.33 | | 11.7 | 34.7 | 5.3 | 23.2 | 9.2 | 13.3 | 2.9 | 2.9 | 20.6 | 68.5 | 0.4 | 2.4 | 14.7 | 2.1 | 113 | <1 | <0.1 | 1.1 | <0.1 | 7 | <0.1 | 11 | 35.8 | 933 | 6.6 | 21.3 | 13.9 | 0.6 | 4.5 | 0.49 | 0.22 | 0.9 | 0.21 | 64.6 | 64.8 | 1.5 | 9.1 |

| Samples | Rb | Sr/Y | (La/Yb)N | (La/Lu)N | (La/Sm)N | LREE | HREE | ΣREE | Ce/Yb | Tb/La | T1 | T3 | T4 |
|---|---|---|---|---|---|---|---|---|---|---|---|---|---|
| HSP-32-4 | 5.9 | 72.94 | 12.81 | – | 4.64 | 14.82 | 5.1 | 19.92 | 34.0 | 0.03 | 0.04 | 0.15 | – |
| HSP-84 | 1.6 | 53.94 | 31.85 | – | 3.84 | 41.92 | 6.0 | 47.92 | 106.5 | 0.02 | 0.23 | 0.26 | – |
| HSP-148 | 2.1 | 0.43 | 0.20 | 0.27 | 0.67 | 19.38 | 190.5 | 209.9 | 0.71 | 0.62 | 0.02 | 0.09 | 0.19 |
| HSP12–10 | 10.1 | 0.53 | 0.55 | 0.58 | 0.80 | 84.31 | 187.4 | 271.7 | 2.36 | 0.25 | 0.16 | 0.11 | 0.10 |

colorless fluorites, Type Ia inclusions were homogenized to liquid at temperatures between 148 °C and 307 °C, and they exhibit final ice melting temperatures at −8.0 °C to −0.5 °C, indicating salinities ranging between 0.9 and 11.7 wt% NaCl equiv. All of the Type Ib inclusions decrepitated prior to final homogenization. Type III inclusions in colorless fluorite exhibit final melting temperatures of clathrates ($T_m$ = 0.2 °C–3.0 °C), indicating salinities ranging between 11.9 and 15.3 wt% NaCl equiv. These inclusions homogenized to vapor at 202 °C–275 °C.

*5.1.2.4. Cu ores.* Fluid inclusions in scheelite with blue luminescence collected from calcite + chalcopyrite + scheelite veins are mainly of Type IIa. These inclusions homogenized by vapor disappearance (463 °C–517 °C) after halite dissolution (250 °C–271 °C). The salinities of these inclusions range from 34.7 to 36.0 wt% NaCl equiv. Fluid inclusions in calcite collected from calcite + chalcopyrite + scheelite veins are mainly Type Ia inclusions. These inclusions exhibit final ice melting temperatures at −15.2 °C to −3.0 °C, indicating salinities of 4.9–18.8 wt% NaCl equiv. They homogenized to liquid at temperatures between 169 °C and 275 °C.

### 5.2. Rare earth and other trace elements

Fourteen fluorite samples of different colors (purple, green, and colorless) and four calcite samples were selected for analysis of REEs and other trace elements. The results are listed in Tables 4 and 5. REEs are normalized to chondrite (Sun and McDonough, 1989).

#### 5.2.1. Fluorite

The total REE concentrations of fluorite from W–Mo, Pb–Zn, and Cu ores range from 0.95 to 200.51 ppm, 9.89 to 244.43 ppm, and 369.35 to 448.19 ppm, respectively (Table 4). There is a large difference in the ΣREE concentrations between the fluorites of different colors collected from the same ore type. For example, purple fluorite, colorless fluorite, and green fluorite from W–Mo skarn ores have ΣREE concentrations of 13.61, 20.29, and 200.51 ppm, respectively. There is no obvious correlation between the REE concentrations and the color of the fluorite or the type of ore. Chondrite-normalized REEs exhibit weak negative Ce (0.85–0.99) anomalies (except for samples HSP247-2 and HSP211-1) and strong negative Eu (0.02–0.44) anomalies (Fig. 12A).

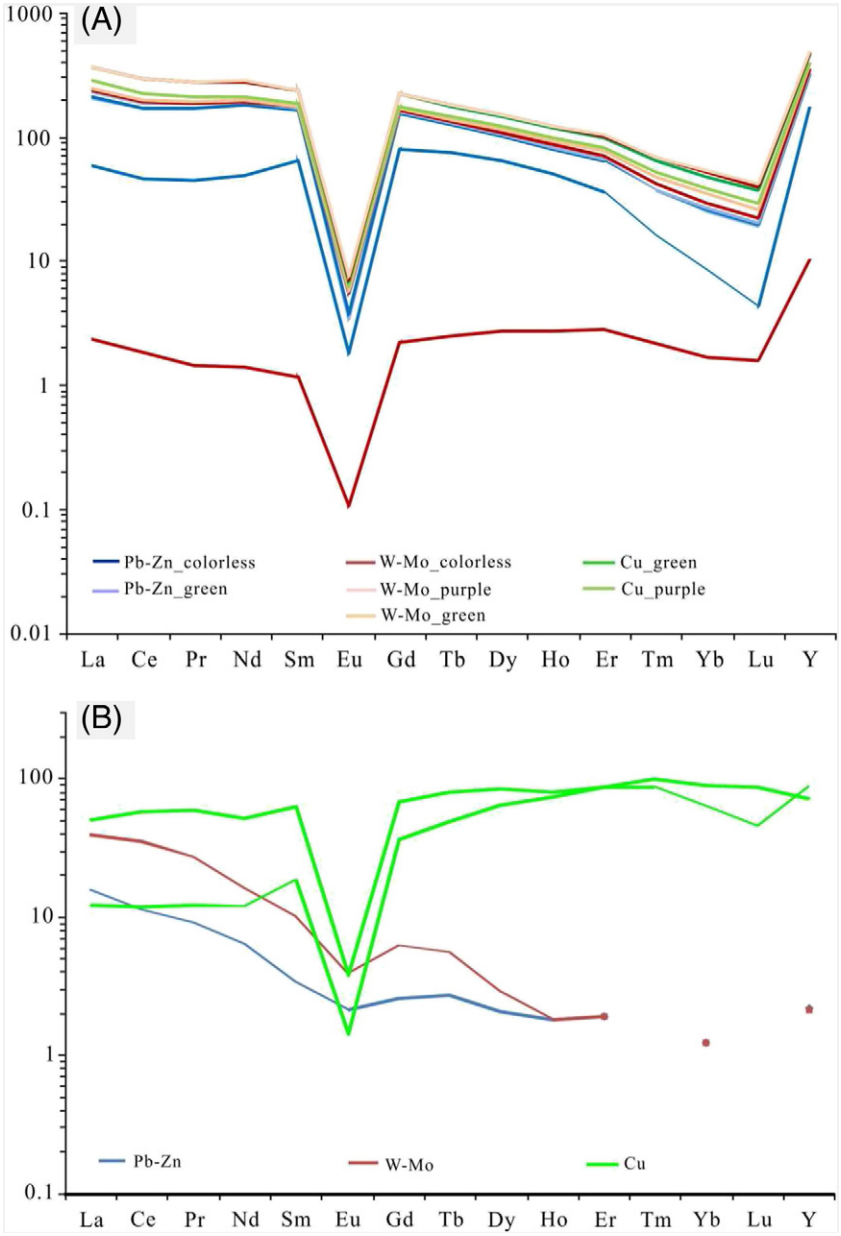


**Fig. 12.** REE patterns of fluorite (A) and calcite (B) collected from W–Mo, Pb–Zn, and Cu ores of the Huangshaping deposit.

*5.2.2. Calcite*

Calcite samples in the Huangshaping deposit contain lower concentrations of REEs (47.92–271.7 ppm) than fluorite (Table 5). Calcites from W–Mo and Pb–Zn ores have the lowest ΣREE concentrations, whereas those from Cu ores show the highest ΣREE concentrations. The chondrite-normalized REEs of the calcites show distinct patterns (Fig. 12B). Calcites from the Cu ores are richer in heavy REEs (HREEs) than the calcites from the W–Mo and Pb–Zn ores. The Cu ores show values of $(La/Sm)_N$ (3.84–4.64) > 1, Eu anomalies ($Eu/Eu^*$ = 0.73–0.50), and weak Ce anomalies ($Ce/Ce^*$ = 0.95–1.08), with higher Sr/Y ratios (53.94–72.94) and lower La/Yb ratios (0.20–0.55). The W–Mo and Pb–Zn ores show $(La/Sm)_N$ (0.67–0.80) < 1, Eu anomalies ($Eu/Eu^*$ = 0.05–0.06), and weak Ce anomalies ($Ce/Ce^*$ = 0.97–1.06), with lower Sr/Y (0.43–0.53) and Ce/Yb (0.71–2.36) ratios and higher La/Yb (12.81–31.85) and Ce/Yb (34.0–106.5) ratios. There are also differences in trace element compositions between calcites of Cu ores and calcites of W–Mo and Pb–Zn ores. The calcites from the Cu ores contain higher concentrations of Na, Er, Ho, Bi, As, and Y, whereas those from W–Mo and Pb–Zn ores show higher concentrations of Mn and Sr.

*5.3. Isotopic analyses*

*5.3.1. S and Pb isotopes*

Sulfur isotope compositions from galena, sphalerite, chalcopyrite, pyrrhotite, and molybdenite are listed in Table 6. $\delta^{34}S$ values are 3.0‰–15.0‰ for galena, 5.5‰–17.4‰ for sphalerite, 4.2‰–7.3‰ for chalcopyrite, 6.9‰–16.6‰ for pyrrhotite, and 14.0‰–18.0‰ for molybdenite. However, the $\delta^{34}S$ values of sulfides sampled from deep underground levels (e.g., samples HSP12–10, HSP12–4, and HSP-148) are relatively lower and have a narrower range of variation (4.2‰–7.3‰). Based on equilibrium isotope fractionation curves for sphalerite and galena (Ohmoto and Rye, 1979), sphalerite–galena pairs in samples

**Table 6**
Sulfur and lead isotopic compositions of sulfide, scheelite, calcite, fluorite, feldspar, and wall rocks at the Huangshaping Deposit, South China.

| Sample | Location | Ore type | Mineral | $\delta^{34}S$ (‰) | $Pb^{208}/Pb^{204}$ | $Pb^{207}/Pb^{204}$ | $Pb^{206}/Pb^{204}$ | References |
|---|---|---|---|---|---|---|---|---|
| HSP-107-1 | −136 m level | Galena-sphalerite ore | Galena | 13.7 | 39.00 | 15.45 | 18.48 | |
| HSP-107-2 | −136 m level | Galena-sphalerite ore | Sphalerite | 15.6 | 40.27 | 15.98 | 18.95 | |
| HSP-219 | −96 m level | Sphalerite-pyrrhotite ore | Pyrrhotite | 16.6 | 39.89 | 15.69 | 18.75 | |
| HSP-219 | −96 m level | Sphalerite-pyrrhotite ore | Sphalerite | 16.2 | 39.47 | 16.11 | 18.88 | |
| HSP-136 | −16 m level | W-Mo-bearing skarn | Molybdenite | 18.0 | 39.71 | 15.95 | 19.21 | |
| HSP-131 | −16 m level | Sphalerite-pyrrhotite ore | Pyrrhotite | 13.3 | 38.74 | 15.55 | 18.81 | |
| HSP-131 | −16 m level | Sphalerite-pyrrhotite ore | Sphalerite | 15.5 | 38.68 | 15.73 | 18.85 | |
| HSP-135 | −16 m level | W-Mo-bearing skarn | Scheelite | | 39.13 | 15.77 | 19.46 | |
| HSP-33 | 20 m level | Galena-sphalerite ore | Galena | 10.6 | 39.78 | 15.91 | 19.18 | |
| HSP-32-4 | 20 m level | Galena-sphalerite ore | Galena | 10.1 | 39.57 | 15.82 | 19.19 | |
| HSP-32-2-1 | 20 m level | Galena-sphalerite ore | Galena | 10.6 | 39.25 | 15.73 | 18.66 | |
| HSP-32-2-2 | 20 m level | Galena-sphalerite ore | Sphalerite | 13.1 | 38.62 | 15.6 | 18.59 | |
| HSP-247 | 56 m level | W-Mo-bearing skarn | Scheelite | | 38.95 | 15.71 | 18.57 | |
| HSP-200 | 92 m level | W-Mo-bearing skarn | Molybdenite | 14.8 | 39.58 | 15.53 | 18.92 | |
| HSP12–10 | ZK1301 132 m deep | Chalcopyrite-scheelite-calcite vein | Chalcopyrite | 4.2 | 39.56 | 15.9 | 19.38 | |
| HSP12–4-2 | G1501 500 m | Sphalerite-pyrrhotite-calcite vein | Pyrrhotite | 6.9 | 39.9 | 15.84 | 19.01 | |
| HSP12–4-1 | G1501 500 m | Sphalerite-pyrrhotite-calcite vein | Sphalerite | 6.9 | 39.84 | 16.28 | 19.03 | |
| HSP-148 | −176 m level | Pyrrhotite-chalcopyrite ore | Chalcopyrite | 7.3 | 39.39 | 15.85 | 18.88 | This paper |
| HSC-03 | −56 m level | Pb-Zn ore | Galena | 10.7 | 38.99 | 15.74 | 18.56 | |
| HSC-10 | −56 m level | Garnet skarn | Molybdenite | 14.0 | 38.88 | 15.73 | 18.49 | |
| HSC-11 | −56 m level | Garnet skarn | Molybdenite | 14.7 | 39.26 | 15.68 | 18.61 | |
| HSC-13 | −56 m level | Pb-Zn ore | Pyrite | 11.0 | 39.00 | 15.74 | 18.57 | |
| HSC-16 | 20 m level | Mo-bearing skarn | Molybdenite | 14.2 | 38.98 | 15.67 | 18.58 | |
| HSC-17 | 20 m level | Pb-Zn ore | Galena | 15.0 | 39.02 | 15.75 | 18.57 | |
| HSC-18 | 20 m level | Pb-Zn ore | Sphalerite | 8.9 | 38.98 | 15.73 | 18.55 | |
| HSC-21 | 20 m level | Pb-Zn ore | Galena | 10.2 | 38.95 | 15.73 | 18.55 | |
| HSC-22 | 20 m level | Pb-Zn ore | Galena | 3.0 | 39.18 | 15.79 | 18.59 | |
| HSC-27 | 56 m level | Pb-Zn ore | Sphalerite | 16.2 | 39.03 | 15.75 | 18.57 | |
| HSC-28 | 56 m level | Veinlet molybdenite in granite porphyry | Molybdenite | 17.1 | 38.84 | 15.68 | 18.66 | |
| HSC-29 | 56 m level | Pb-Zn ore | Galena | 9.2 | 38.95 | 15.72 | 18.55 | |
| HSC-39 | 20 m level | Pb-Zn skarn ore | Sphalerite | 17.4 | 38.89 | 15.71 | 18.54 | |
| HSC-56 | −16 m level | Pb-Zn skarn ore | Pyrite | 24.2 | 38.90 | 15.71 | 18.53 | |
| HSC-76 | 56 m level | Pb-Zn ore | Sphalerite | 5.5 | 39.16 | 15.78 | 18.60 | |
| HSP129–11 | | Mo-bearing garnet skarn | Molybdenite | 14.0 | 38.77 | 15.69 | 18.53 | Yao et al., 2005; |
| BSC-22A | −70-119# | Cu ores | Chalcopyrite | | 39.13 | 15.76 | 18.67 | Zhu et al., 2012 |
| HSP-32-4 | 20 m level | Pb-Zn ore | Calcite | | 38.93 | 15.72 | 18.56 | |
| HSP-84 | −176 m level | W-Mo-bearing skarn | Calcite | | 38.82 | 15.73 | 18.45 | |
| HSP-148 | −176 m level | Pyrrhotite-chalcopyrite ore | Calcite | | 38.91 | 15.72 | 18.56 | |
| HSP12–10 | G1501 | Chalcopyrite-scheelite-bearing Calcite vein | Calcite | | 38.98 | 15.74 | 18.67 | |
| HSP-84–1 | −176 m level | W-Mo-bearing skarn | Purple fluorite | | 38.95 | 15.73 | 18.59 | |
| HSP-84–2 | −176 m level | W-Mo-bearing skarn | Colorless fluorite | | 38.87 | 15.70 | 18.53 | |
| HSP-84-3 | −176 m level | W-Mo-bearing skarn | Green fluorite | | 38.88 | 15.72 | 18.49 | |
| HSP-107-2 | −136 m level | Pb-Zn ore | Colorless fluorite | | 38.95 | 15.72 | 18.55 | |
| HSP-107-3 | −136 m level | Pb-Zn ore | Green fluorite | | 38.96 | 15.72 | 18.61 | |
| HSP-33-2 | 20 m level | Pb-Zn-Ag ore | Colorless fluorite | | 38.92 | 15.71 | 18.53 | |
| HSP-33-3 | 20 m level | Pb-Zn-Ag ore | Green fluorite | | 39.01 | 15.72 | 18.54 | |
| HSP-28-2 | 56 m level | W-Mo ore | Colorless fluorite | | 38.58 | 15.79 | 18.89 | |
| HSP-28-3 | 56 m level | W-Mo ore | Green fluorite | | 38.90 | 15.73 | 18.92 | |
| HSP-211-1 | −96 m level | W-Mo ore | Purple fluorite | | 39.08 | 15.74 | 18.82 | |
| HSP-211-3 | −96 m level | W-Mo ore | Green fluorite | | 39.01 | 15.78 | 18.83 | |
| HSP-135-2 | −16 m level | W-Mo ore | Colorless fluorite | | 38.79 | 15.66 | 18.81 | |
| HSP-247-2 | 56 m level | W-Mo ore | Colorless fluorite | | 38.921 | 15.70 | 18.56 | This paper |

**Table 7**
Sm, Nd, C, and O isotopes of calcite, scheelite, and garnet at the Huangshaping Deposit, South China.

| Sample | Ore type | Minerals | $\delta^{18}O$ (‰)$_{SMOW}$ | $\delta^{13}C_{PDB}$ (‰) | Sm (ppm) | Nd (ppm) | $^{147}Sm/^{144}Nd$ | $^{143}Nd/^{144}Nd$ | ±2σ | εNd(t) | $T_{2DM}$(Ga) |
|---|---|---|---|---|---|---|---|---|---|---|---|
| HSP-84 | −176 m level, W-Mo-bearing skarn | Calcite | 13.2 | −1.12 | 1.44 | 6.63 | 0.1312 | 0.512248 | 3 | −6.3 | 1.5 |
| HSP-148 | −176 m level, chalcopyrite ore | Calcite | 11.1 | −4.95 | 3.44 | 6.55 | 0.3174 | 0.512486 | 2 | −5.4 | 1.4 |
| HSP-247 | 56 m level, W-Mo ore | Scheelite | 5.4 | | 20.06 | 64.09 | 0.1892 | 0.512327 | 4 | −5.9 | 1.4 |
| HSP-247 | 56 m level, W-Mo ore | Garnet | | | 2.19 | 9.16 | 0.1442 | 0.512235 | 3 | −6.8 | 1.5 |
| HSP-135 | −16 m level, W-Mo-bearing skarn | Garnet | | | 0.63 | 0.57 | 0.6773 | 0.512818 | 10 | −6.1 | 1.4 |
| HSP-135 | −16 m level, W-Mo-bearing skarn | Scheelite | 6 | | 2.99 | 13.64 | 0.1324 | 0.512259 | 6 | −6.1 | 1.4 |
| HSP12–10 | ZKG1501, chalcopyrite-calcite vein | Calcite | 11.7 | −4.54 | 9.76 | 23.92 | 0.2468 | 0.512415 | 3 | −5.3 | 1.4 |
| HSP12–10 | ZKG1501, chalcopyrite-calcite vein | Scheelite | | | 81.69 | 332.27 | 0.1486 | 0.512440 | 5 | −2.9 | 1.2 |
| HSP-32-4 | 20 m level, Pb-Zn ore | Calcite | 13.5 | −1.48 | | | | | | | |

HSP107 and HSP32-2 collected from Pb–Zn ores are used to calculate the temperature, which yields 334 °C and 256 °C, respectively.

Lead isotope compositions were obtained from 18 sulfide samples, 4 calcite samples, and 14 fluorite samples (Table 6). Lead isotope compositions for sulfide, calcite, and fluorite exhibit a large range of variation. $^{206}Pb/^{204}Pb$, $^{207}Pb/^{204}Pb$, and $^{208}Pb/^{207}Pb$ values for sulfides range from 18.48 to 19.46, 15.45 to 16.28, and 38.62 to 40.27, respectively. Calcite exhibits narrower ranges from 18.45 to 18.67, 15.72 to 15.74, and 38.82 to 38.98, respectively, whereas fluorite exhibits wider ranges from 18.50 to 18.90, 15.66 to 15.79, and 38.59 to 39.08, respectively. There exists no obvious correlation between lead isotope compositions and the colors of fluorite or types of ore.

#### 5.3.2. C and O isotopes

Four calcite samples were used to determine their carbon and oxygen isotope compositions (Table 7). All samples are associated with the ores. Calcite from the Cu ores (samples HSP-148 and HSP12–10) have $\delta^{18}O = +11.1‰$ to $+11.7‰$ and $\delta^{13}C = -4.95$ to $-4.54‰$, respectively. However, the calcite sample from the W–Mo skarn ores has $\delta^{18}O = 13.2‰$ and $\delta^{13}C = -1.12‰$, and calcite from Pb–Zn ores has $\delta^{18}O = 13.5‰$ and $\delta^{13}C = -1.48‰$. These values are different from those of either Carboniferous carbonate rock ($\delta^{18}O = 13.46‰$–$14.76‰$ and $\delta^{13}C = -2.9$ to $-2.4‰$) or the calcite from quartz porphyry ($\delta^{18}O = 13.67‰$ and $\delta^{13}C = -1.4‰$) or the granite porphyry ($\delta^{18}O = 13.95‰$ and $\delta^{13}C = -1.2‰$) (Zhang et al., 2012). $\delta^{18}O$ values of hydrothermal fluids responsible for formation of calcite were calculated based on analysis of fluid inclusions in calcite (Zheng, 1993; Sheppard and Gilg, 1996). As a result, $\delta^{18}O$ values of 8.10‰, 8.41‰, and 4.34‰–4.96‰ were obtained for hydrothermal fluids for the W–Mo, Pb–Zn, and Cu ores, respectively.

Two scheelite samples collected from W–Mo ores were also analyzed (Table 7). Their $\delta^{18}O$ value ranges from 5.4‰ to 6‰. The $\delta^{18}O$ value of hydrothermal fluids responsible for the formation of scheelite was calculated at a median temperature based on analysis of fluid inclusions in scheelite (Zheng, 1993; Sheppard and Gilg, 1996). The obtained $\delta^{18}O$ value for fluids ranges from 8.61‰ to 9.21‰, similar to the $\delta^{18}O$ compositions of hydrothermal fluids that produced calcite in the W–Mo skarn ores.

#### 5.3.3. Sm–Nd isotopes

Sm–Nd isotope compositions of calcite, scheelite, and garnet are listed in Table 7. Among the three minerals, garnet has the lowest concentrations of Sm (0.63–2.19 ppm) and Nd (0.57–9.16 ppm), whereas scheelite has the highest concentrations of Sm (2.99–81.69 ppm) and Nd (13.64–332.27 ppm). The $\varepsilon_{Nd}(t)$ values range from −6.8 to −5.4 for calcite, −6.1 to −2.9 for scheelite, and −6.8 to −6.1 for garnet. The three minerals have similar two-stage Nd model ages ($T_{2DM}$) of 1.4 Ga except for scheelite sample HSP12–10 (whose age was 1.1 Ga).

## 6. Discussion

### 6.1. Interpretation of fluorite and calcite REE data

Gangue minerals of hydrothermal ore deposits provide important information about the condition and process of mineralization. Generally, hydrothermal fluids that produce gangue minerals are in near equilibrium with ore minerals at the time of mineralization (Barnes, 1997). Fluorite and calcite are two important gangue minerals found within the Huangshaping deposit. Their geochemical features can help to reveal the chemical composition of hydrothermal fluids. REE patterns of fluorite and calcite are also helpful for characterizing the evolution of hydrothermal fluids (Jebrak et al., 1985; Constantopoulos, 1988; Morozov et al., 1996; Graupner et al., 1999; Möller and Dulski, 1999; Trinkler et al., 2005; Li et al., 2014a).

The REE contents (0.95–448.19 ppm) of fluorites of different colors vary considerably, yet they display no distinguishable patterns (Fig. 12A) for different types of ore (i.e., W–Mo, Pb–Zn, and Cu ores). Ce/Yb and Tb/La ratios in fluorite from the deposit also vary considerably among different types of ore, suggesting a complicated history for fluorite precipitation (Constantopoulos, 1988). The Y/Ho ratio of fluorite in different colors ranges from 47 to 163, indicating the involvement of another source with a higher Y/Ho ratio (other than marine sedimentary rocks that have Y/Ho = 40–80; Bau and Dulski, 1996) in the mineralization process.

The REE characteristics of hydrothermal calcite are controlled by the composition of ore-forming fluids and physicochemical conditions during its precipitation (Bau and Möller, 1992). Fluids with temperature > 230 °C percolating through different rock types may show similar REE patterns (Michard, 1989). Calcite samples collected from W–Mo, Pb–Zn, and Cu ores in the Huangshaping deposit show large discrepancies in their REE patterns (Fig. 12B) and some trace element features. Calcite associated with Cu ores is rich in Na, K, Y, ΣREE, and especially HREE and has higher Tb/La ratios, whereas the calcite associated with W–Mo and Pb–Zn ores is richer in Mn and Sr,

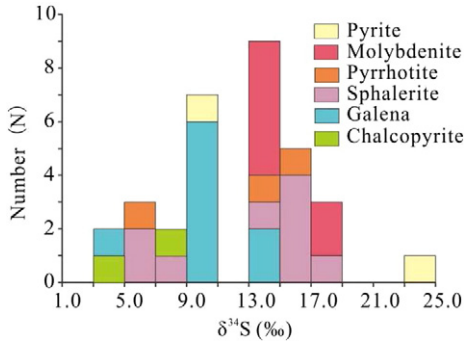


**Fig. 13.** Histogram of S isotopes of sulfides from the Huangshaping deposit.

depleted in HREE, and has higher δEu and higher La/Yb, La/Sm, and Ce/Yb ratios. This suggests that the fluids for W–Mo and Pb–Zn mineralization were different from the fluids for Cu mineralization in the Huangshaping deposit.

The Y/Ho ratios in calcite range from 25 to 33 in Cu ores. This may suggest that the Cu-related calcite was likely precipitated from magma because generally igneous carbonate has a Y/Ho ratio of 23–33 (Bau and Dulski, 1996). Y/Ho ratios in calcite from W–Mo and Pb–Zn ores range from 33 to 34, which is consistent with hydrothermal carbonate being derived from the limestone/dolomite and magma (since seawater Y/Ho = 40–80; Bau and Möller, 1992).

### 6.2. Interpretation and implications of isotopic data

Sulfur isotope compositions of sulfides vary considerably among different ores from the Huangshaping deposit ($\delta^{34}S$ = 3.0‰–18.0‰; Table 6, Fig. 13), similar to the sulfur isotopic data reported by Tong et al. (1986); Xi et al. (2009), and Zhu et al. (2012). The large variation of $\delta^{34}S$ values suggests multi-sourced sulfur involved in the mineralization. Previous studies indicated that the sulfur derived from granite porphyry and the Carboniferous Formation (Tong et al., 1986), and the mixture of magma and the Carboniferous Formation (Xi et al., 2009). Zhu et al. (2012) suggested that the high $\delta^{34}S$ value of sulfides in the

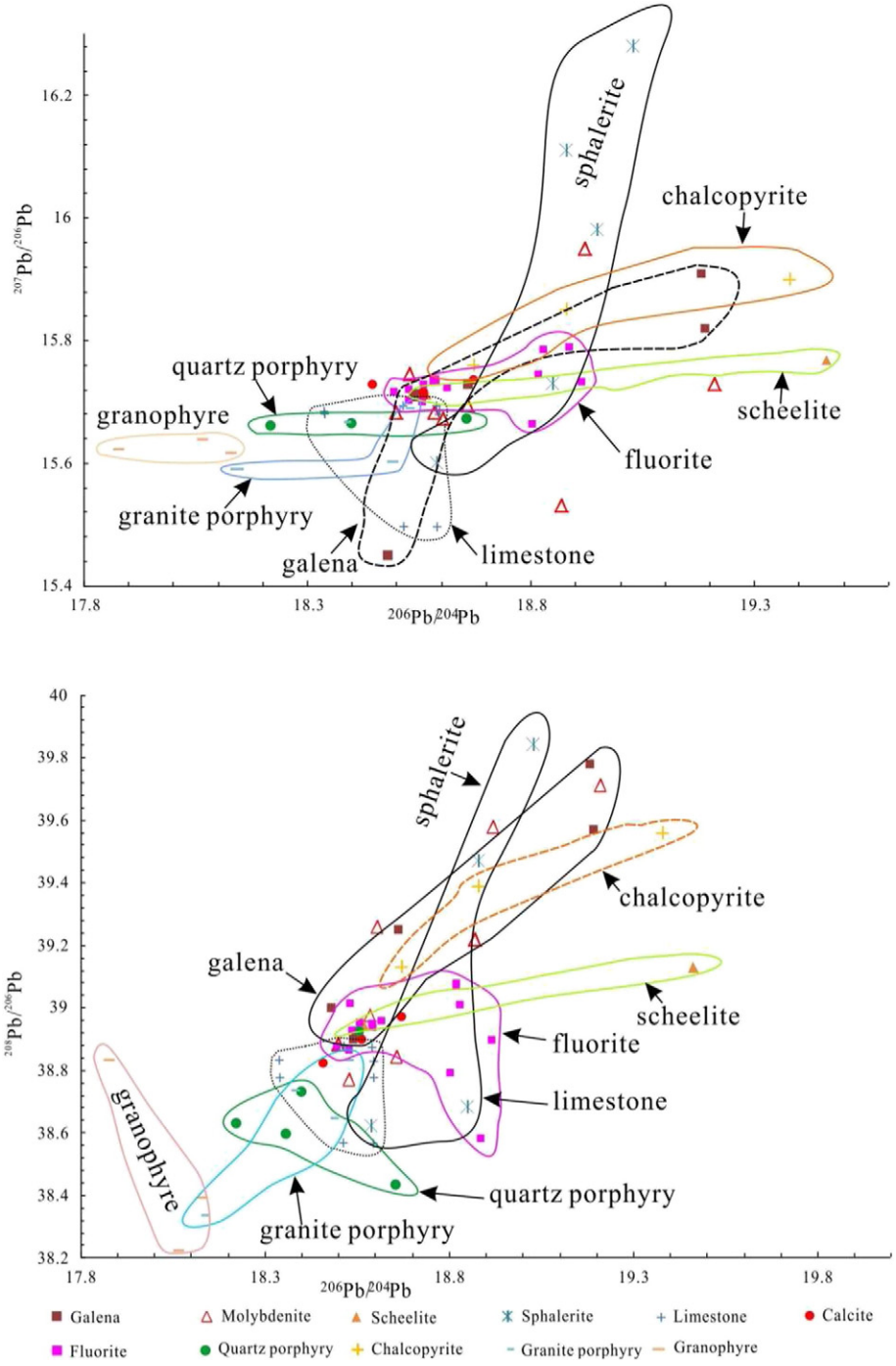


**Fig. 14.** Diagrams of $^{206}Pb/^{204}Pb$–$^{207}Pb/^{206}Pb$ (A) and $^{206}Pb/^{204}Pb$–$^{208}Pb/^{204}Pb$ (B) from sulfides, oxides, granite, and limestone (wall rock) from the Huangshaping deposit. (Data sources: Tong et al. (1986); Yao et al. (2005); Zhu et al. (2012), and this study).

Huangshaping deposit is derived from high-$\delta^{34}S$ magma, but they regarded the higher $\delta^{34}S$ value of molybdenite in quartz–molybdenite vein as the high-$\delta^{34}S$-value magma, but this is impossible because the sulfur isotope of molybdenite from quartz–molybdenite vein cannot represent the sulfur isotope composition of magma even with molybdenite precipitation at the high temperature. Recently, Yuang et al. (2013) obtained $\delta^{34}S$ values of quartz porphyry ranging from 4.8‰ to 7.5 ‰ and for granite porphyry ranging from 4.9‰ to 11.4 ‰. These $\delta^{34}S$ values also support the fact that magma $\delta^{34}S$ values are not as high as that for molybdenite.

Sulfur isotope composition of the ore is sometimes strongly affected by host sedimentary rocks, especially by evaporite sulfur with a much higher $\delta^{34}S$ value and partly by biogenic sulfur with a low $\delta^{34}S$ value. The $\delta^{34}S$ values higher than the magmatic value of +1 per mil are considered to result from (1) seawater sulfate brought up to granitic magmas by subduction processes (Sasaki and Ishihara, 1979; Ueda and Sakai, 1984), (2) fossilized sulfate of evaporite beds assimilated into the magmas within the continental crust (Zhou and Yue, 1996), or (3) minor amounts of structurally substituted sulfate contained in carbonate beds recycled into the granitic magmas or directly mixing with the ore solution (Ishihara et al., 2003). In the Late Jurassic, the Huangshaping deposit was far from the subduction zone, so it is impossible for seawater sulfate to be involved in the magma and the mineralization. The normal $\delta^{34}S$ values of porphyries also indicate that no sulfate from the evaporiteunits is involved in the magma emplacement. Carbonate rocks from the Huangshaping mine have the higher $\delta^{34}S$ values of sulfate, with sulfur ranging from 17.0‰ to 25.7‰ (Ishihara et al., 2003). The high $\delta^{34}S$ values are considered to originate in the carbonate from the interaction of the ore fluids with the sedimentary wall rock. The high $\delta^{34}S$ values of sulfide appear at the contact zone between the porphyries and the Carboniferous limestone and dolomite; beyond this zone, the sulfide shows increasing richness in $^{32}S$. This also suggests that sulfur fractionation in the oxidizing environment during W–Mo mineralization and in the reducing environment during Pb–Zn mineralization should be considered. At the deep level (samples HSP12–10, HSP12–4, and HSP-148), the sulfides with Cu mineralization have lower $\delta^{34}S$ values, indicating a fluid rich in $^{32}S$ in Cu mineralization; the sulfur isotopic fractionation in the more reducing environment and the little carbonate sulfur involved in the Cu mineralization are considered for sulfur isotopes composition during the Cu mineralization.

As shown in the $^{207}/^{204}Pb$ vs. $^{206}Pb/^{204}Pb$ and $^{208}/^{204}Pb$ vs. $^{206}Pb/^{204}Pb$ diagrams in Fig. 14, the lead isotopic compositions of fluorite, calcite, chalcopyrite, pyrrhotite, sphalerite, galena, scheelite, and molybdenite give the scatter data, which do not coincide well with the range for Late Jurassic porphyries (quartz porphyry, granite porphyry, and granophyre). It is also clear that the lead isotopes for other rocks present in the mining areas (e.g., Devonian limestone and Carboniferous limestone and dolomite) are significantly different from those of the sulfides and Late Jurassic porphyryies. Sphalerite exhibits a narrow range of $^{206}Pb/^{204}Pb$ but a wide range of $^{207}Pb/^{204}Pb$ and $^{208}Pb/^{204}Pb$ isotopic compositions, which is different from those for galena, chalcopyrite, and scheelite. The lead isotopic composition of galena, chalcopyrite, and scheelite show a binary lead mixture. More radiogenic $Pb^{206}$-, $U^{238}$-, and $Th^{232}$-rich rocks occurring at deeper levels of the crust were considered during the Pb–Zn mineralization. Thus the ore-forming metals are considered to be related to the Late Jurassic porphyries and host wall rocks, while radiogenic $Pb^{206}$-, $U^{238}$-, and $Th^{232}$-rich rocks have also made contribution to the mineralization.

The Mesozoic felsic intrusions in the deposit have higher Cu, Pb, Zn, Sn, and Mo concentrations than global felsic plutons (Shi et al., 1996). For example, the granite porphyry of the Huangshaping deposit has 571 ppm Zn, 803 ppm Cu, and 83 ppm Sn, suggesting that the magmas likely provided metals during the mineralization process. The Shidengzi Formation limestone of the deposit has Cu, Pb, Sn, Mo, and Bi concentrations similar to those of the limestone distal from the deposit. At both the deposit and regional scales, there exist no measurable depletions in Cu, Pb, Mo, and Bi but is some depletion in Zn (Shi et al., 1996). Therefore, Zn might be partly sourced from local sedimentary rocks whereas Cu, Pb, and W would be from magmas. A similar situation has been documented for intrusive rocks in other carbonate-replacement systems (e.g., the San Martin mineral district of Mexico (Graf, 1997) and the Lavrion mineral district of Greece (Bonsall et al., 2011)).

In the $\delta^{13}C$ vs. $\delta^{18}O_{SMOW}$ diagram (Fig. 15), nonmineralized limestone of the Huangshaping deposit has $\delta^{13}C$ and $\delta^{18}O$ values of 0.1‰–2.3‰ and 17.6‰–22.9‰, respectively, which are typical values for marine limestone (Bowman, 1998). Mineralized limestone shows

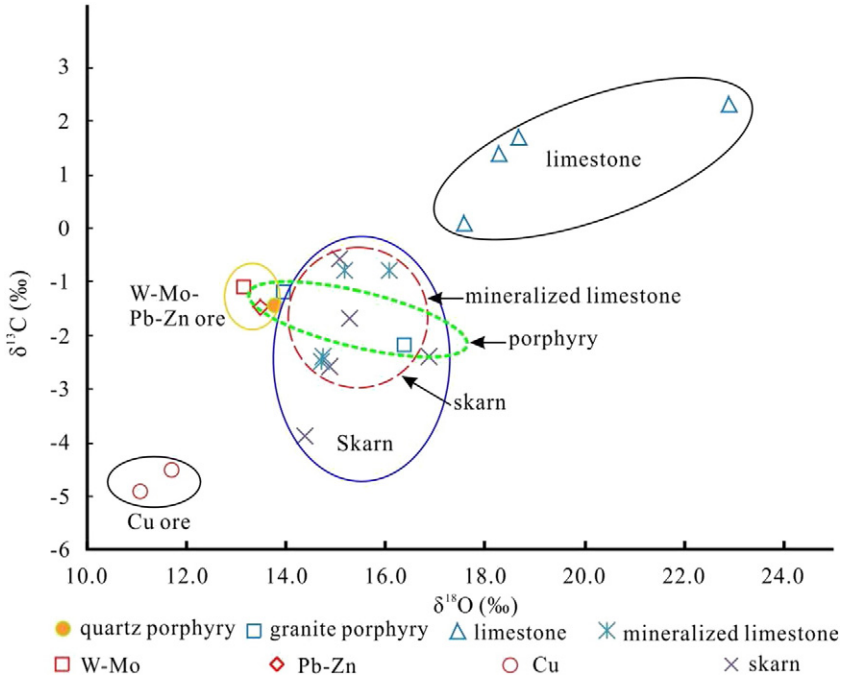


**Fig. 15.** Diagram of $\delta^{18}O$ vs. $\delta^{13}C$ for calcite collected from different types of ores and rocks from the Huangshaping deposit. (Data sources: mineralized limestone: Tong et al. (1986) and Zhang et al. (2012); nonmineralized limestone: Zhang et al. (2012); granite porphyry, quartz porphyry, and skarns: Zhang et al. (2012); other data: this study).

relatively lighter compositions of $\delta^{13}C$ and $\delta^{18}O$. The calcite data collected from W–Mo and Pb–Zn ores plot near the calcite collected from nonmineralized limestone, quartz porphyry, and granite porphyry, suggesting their possible generic relationship. However, calcite from Cu ores has distinctly lower $\delta^{18}O$ and $\delta^{13}C$ values (Fig. 15), possibly indicating involvement of another fluid system.

The $\delta^{18}O$ values of the fluids responsible for the formation of the calcite collected from the W–Mo, Pb–Zn, and Cu ores are 8.10‰, 8.41‰, and 4.34‰–4.96‰, respectively. The data suggest that meteoric water might be involved in the W–Mo and Pb–Zn mineralization.

As shown in the $\varepsilon_{Nd}(t)$ vs. $^{206}Pb/^{204}Pb$, $\varepsilon_{Nd}(t)$ vs. $^{207}Pb/^{204}Pb$, and $\varepsilon_{Nd}(t)$ vs. $^{208}Pb/^{204}Pb$ diagrams in Fig. 16, quartz porphyry and granophyre have similar $\varepsilon_{Nd}(t)$ values, and granite porphyry has lower $\varepsilon_{Nd}(t)$ values, although the $T_{2DM}$ values are similar. Quartz porphyry, granophyre, and granite porphyry have narrow ranges of $^{206}Pb/^{204}Pb$ values. Granite porphyry has a wide range of $^{207}Pb/^{204}Pb$ and $^{208}Pb/^{204}Pb$ values. Calcite associated with Cu mineralization has $\varepsilon_{Nd}(t)$ values (−6.3 to −5.4) similar to that of the calcite (−6.3) associated with W–Mo mineralization. The $\varepsilon_{Nd}(t)$ values (−6.1 to −5.9) of scheelite collected from W–Mo ores are similar to those for garnet (−6.8 to −6.1). The higher values of $^{206}Pb/^{204}Pb$, $^{207}Pb/^{204}Pb$, and $^{208}Pb/^{204}Pb$ for calcite and scheelite than for quartz porphyry, granophyre, and granite porphyry indicate a more mature crustal contribution and more radiogenic $Pb^{206}$, $U^{-238}$, and $Th^{232}$-rich crustal involvement in the mineralization process. The scheelite collected from calcite + chalcopyrite + scheelite veins has a higher $\varepsilon_{Nd}(t)$ value (−2.9) than the scheelite from skarn W–Mo ores (−6.9 to −6.0), suggesting that more mantle-derived materials were involved in the precipitation of the Cu ores.

### 6.3. Sources and evolution of ore-forming fluids

The regional NNE-striking CCLDF zone was reactivated by local crustal extension during the Late Jurassic (Bai et al., 2008; Hu and Zhou, 2012). Such extension allowed generation of local-scale faults and significant ascent and emplacement of granitic magmas into the shallow crust, producing stocks of granodiorite porphyry, quartz porphyry, and granite porphyry (Bai et al., 2008). In addition to exposed granitoids stocks, the aeromagnetic data (Li et al., 2014b) reveal the existence of a large number of unexposed granitic intrusions in that region. Hydrothermal fluids rich in ore-forming elements exsolved from the magmas could be involved in the mineralization process (Shinohara and Hedenquist, 1997; Meinert et al., 2003, 2005; Heinrich, 2005).

The Huangshaping deposit is an example of a mineralized magmatic–hydrothermal complex system with high-potassic calc-alkalic affinity. Fluid inclusions analyzed in calcite, fluorite, actinolite, molybdoscheelite, and scheelite suggest involvement of F–$CO_2$-rich magmatic fluids in major hydrothermal-mineralization stages. Minerals such as garnet, actinolite, and molybdoscheelite were formed from high-temperature and high-salinity fluids of magmatic origin in the early stage. The oxygen isotopes of calcite and scheelite also suggest involvement of magmatic fluids in the W–Mo, Pb–Zn, and Cu mineralization.

An interpretation of the fluid evolution of the Huangshaping hydrothermal system is illustrated in Fig. 17, which shows the pressure–temperature paths of different flowing fluids characterized by the coexistence of various fluid inclusions (Fig. 11) and C–O–S–Pb–Nd isotopic data. Episodic fluid activities resulted in crystallization of skarn minerals and subsequent precipitation of ore minerals.

Large volumes of magmas were emplaced in the upper crust by subduction of the Pacific Plate (Li et al., 2008) during the Late Jurassic as evidenced by reported ages of the granite porphyries in the district (Yao et al., 2005; Yuan et al., 2014). As the magmas cooled and crystallized at depths of 4 to 5 km (Fig. 17), the melts were eventually saturated with respect to aqueous fluids, a source of supercritical fluids with a moderate salinity of 6–8 wt% NaCl equiv. (Bodnar, 1995). Subsequent ascent of the magmatic fluids to shallower depths probably was concurrent with emplacement of granite porphyry dikes to ≈2–3 km beneath the paleosurface. The magmatic fluids with a bulk salinity of 7 wt% NaCl equiv. evolving along Path I would intersect its solvus at a 2-km depth and separate into a 45 wt% hypersaline liquid in equilibrium with a vapor containing 1 wt% NaCl equiv. (Fig.17); the majority of skarn minerals were precipitated from the hypersaline fluids.

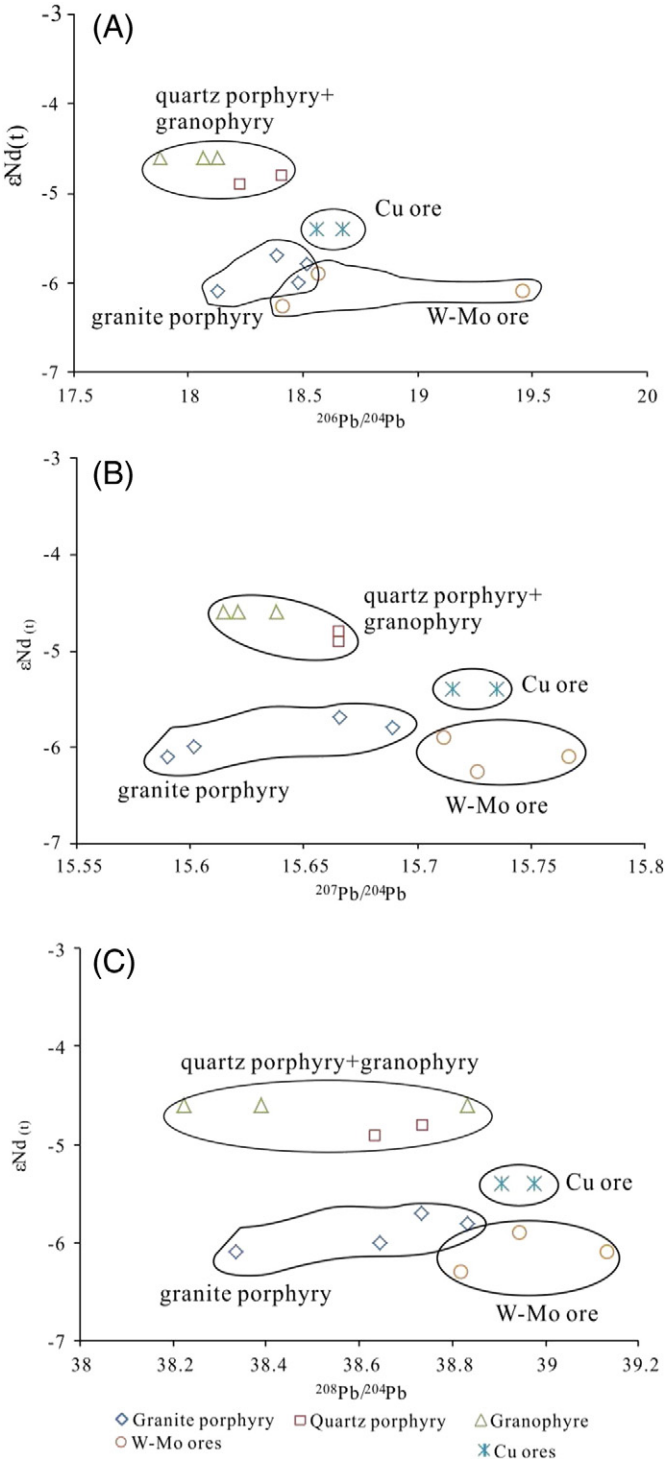


**Fig. 16.** Diagrams of $\varepsilon_{Nd}(t)$–$^{206}Pb/^{204}Pb$ (A), $\varepsilon_{Nd}(t)$–$^{207}Pb/^{204}Pb$ (B), and $\varepsilon_{Nd}(t)$–$^{208}Pb/^{204}Pb$ (C) for calcite, garnet, and scheelite. (Data sources for quartz porphyry, granite porphyry, and granophyry are from Yao et al. (2007).)

Subsequent fluids exsolved from the underlying vapor-saturated magma chamber followed cooling Path II (Fig. 17). Because of the lower rate of advection (Shinohara and Hedenquist, 1997), the subsequent fluids cooled sufficiently during ascent and never intersected their solvus (Fig. 17). Cooling to a temperature below ≈450 °C resulted in a transition from ductile to brittle deformation behavior, causing a change from lithostatic to hydrostatic conditions (Fournier, 1991). The fluids with 7 wt% NaCl equiv. intersected the saturated vapor-pressure curve at 400 °C, resulting in boiling of the ascending fluids and the molybdscheelite precipitation. With an increase in reduction and decrease in oxidation, hydrothermal fluids ($\delta^{18}O$ = 8‰–10‰) rich in $CH_4$ and $CO_2$ experienced boiling and separation of molybdenum and tungsten, forming Mo-free scheelite and molybdenite-bearing quartz veins. With a continued decrease in temperature and fluid-wall rock reaction, the ore fluids became more reductive and interacted with sedimentary wall rock, so that Pb and Zn sulfides precipitated from the fluids, forming Pb–Zn ores.

Subsequent deep-rooted magma experienced a further differentiation to produce Cu-rich magmatic fluids ($\delta^{18}O$ = 4‰–5‰). With a decrease of temperature and pressure, chalcopyrite and calcite were precipitated at 270 °C and above along Path III.

## 7. Conclusions

The Huangshaping deposit contains three types of ores or mineralization: W–Mo, Pb–Zn, and Cu. The ore and gangue minerals contain three types of fluid inclusions: aqueous liquid–vapor inclusions, daughter-mineral-bearing aqueous inclusions, and $H_2O$–$CO_2$ inclusions. Fluid inclusion data obtained in this study suggest two sources of ore-forming fluids responsible for the W–Mo, Pb–Zn, and Cu mineralization.

Calcite samples collected from the W–Mo, Pb–Zn, and Cu ores show different chondrite-normalized REE patterns. Calcites from the Cu ores are rich in HREE, Na, Bi, and As, whereas calcites from the W–Mo and Pb–Zn ores contain higher amounts of Mn and Sr, indicating different sources of fluids involved in the W–Mo, Pb–Zn, and Cu mineralization.

Sulfur isotopes from galena, sphalerite, chalcopyrite, pyrrhotite, and molybdenite reveal two sources of hydrothermal fluids involved in the mineralization as well. The W–Mo and Pb–Zn ores contains sulfides with higher $\delta^{34}S$ values whereas the Cu ores contain sulfides with relatively lower $\delta^{34}S$ values. The lead isotope data for sulfides, fluorite, calcite, and scheelite also show different origins for the metals W, Mo, Pb, Zn, and Cu. The Sm–Nd isotopic analysis of scheelite, garnet, and calcite suggests more mantle-derived materials involved in the Cu mineralization.

We conclude that two sources of ore-forming fluids were involved in the formation of the Huangshaping W–Mo–Pb–Zn–Cu magmatic–hydrothermal deposit. The first one was derived from granite porphyry magmas and was responsible for the W–Mo and then Pb–Zn mineralization during its evolution from magmatic phase to magmatic–meteoritic mixing. The second was derived from the deep-rooted magma and contributed to the Cu mineralization.

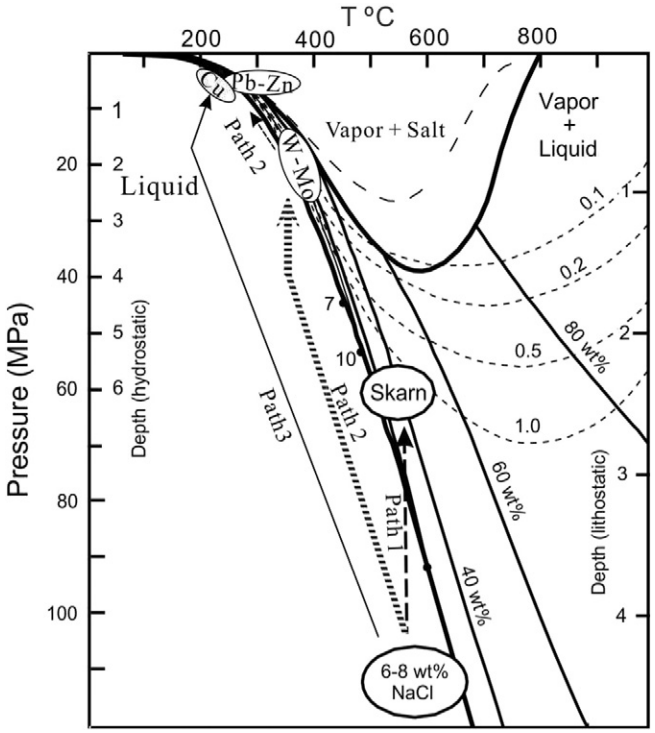


**Fig. 17.** Fluid evolution temperature–pressure paths for the Huangshaping deposit (after Fournier, 1987). Isopleths of NaCl in liquid (dark lines) and vapor (light lines) are shown for compositions of interest. Three cooling paths are shown for an initial liquid composition of 7 wt% NaCl equiv. Fluids ascending along Path I reach solvus at ~600 °C and under a pressure of 540 bar (a lithostatic pressure at a depth of about 2 km). Continued depressurization results in separation of a small amount of hypersaline liquid with a low-salinity vapor dominating the mass of the two-phase fluids. The later fluids ascending along Path II intersect the saturated vapor-pressure curve at ~400 °C and under a hydrostatic pressure of 200 bar, which is also equivalent to a depth of about 2 km. With continued cooling, molybdscheelite, molybdenite, and Pb–Zn minerals consequently precipitate. Another source of magmatic fluids ($\delta^{18}O$ = 4‰–5‰) derived from lower crust mafic magmas were evolved along Path III, resulting in precipitation of Cu minerals such as chalcopyrite.

## Acknowledgments

This study was financially supported by the National Fundamental Research and Development Program of China (Grant No. 2012CB416705) and the National Natural Science Foundation of China (Grant No. 41272112). We thank Liubai Gong and Fuchun Li for their assistance in our field seasons. We are grateful to Lawrence Meinert, Timothy Baker, Franco Pirajno, and two anonymous reviewers for their comments and suggestions that significantly helped to improve the original manuscript.

## References

Audétat, A., Günther, D., 1999. Mobility and H2O loss from fluid inclusions in natural quartz crystals. Contrib. Mineral. Petrol. 137 (1–2), 1–14.

Bai, D.Y., Huang, J.Z., Li, J.D., 2007. Multiple geological elements constraint on the Mesozoic tectonic evolution of south China: apocalypse of the Mesozoic geological evolution in southeastern Hunan and the Hunan–Guangdong–Jiangxi border area. Geofis. Meteorol. 31 (1), 1–13.

Bai, D.Y., Ma, T.Q., Wang, X.H., Zhang, X.Y., Chen, B.H., 2008. Progress in the study of Mesozoic tectono-magmatism and mineralization in the central segment of the Nanling Mountains—summary of major achievements of the 1:250,000 geological survey in southeastern Hunan. Geol. China 35 (3), 436–454.

Baker, T., Lang, J.R., 2003. Reconciling fluid inclusion types, fluid processes, and fluid sources in skarns: an example from the Bismark Deposit. Mexico: Mineralium Deposita, 38, 474–495.

Bakker, R.J., 1997. CLATHRATES: computer programs to calculate fluid inclusion V-X properties using clathrate melting temperatures. Comput. Geosci. 23, 1–18.

Barnes, H.L., 1997. Geochemistry of Hydrothermal Ore Deposits. third ed. John Wiley and Sons, New York, p. 972.

Bau, M., Dulski, P., 1996. Comparative study of yttrium and rare-earth element behavior in fluorite-rich in hydrothermal fluids. Contrib. Mineral. Petrol. 119, 213–223.

Bau, M., Möller, P., 1992. Rare earth element fractionation in metamorphogenic hydrothermal calcite, magnesite and siderite. Mineral. Petrol. 45, 231–246.

Bodnar, R.J., 1993. Revised equation and table for determining the freezing point depression of $H_2O$–NaCl solutions. Geochim. Cosmochim. Acta 57, 683–684.

Bodnar, R.J., 1995. Fluid-inclusion evidence for a magmatic source for metals in porphyry copper deposits. In: Thompson, J.F.H. (Ed.), Magmas, Fluids, and Ore Deposits. Vol. 23 of Short Course Series: Ottawa, Canada, Mineralogical Association of Canada, pp. 139–152.

Bonsall, T.A., Spry, P.G., Voudouris, P.Ch., Tombros, S., Seymour, K., Melfos, V123., 2011. The geochemistry of carbonate-replacement Pb–Zn–Ag mineralization in the Lavrion district, Greece: fluid inclusion, stable isotope, and rare earth element studies. Econ. Geol. 106, 619–651.

Bowman, J.R., 1998. Stable-isotope systematics of skarns. In: Lentz, D.R., Thompson, J.F.H. (Eds.), Mineralized Intrusion Related Skarn SystemsVol. 26 of Short Course Series. Mineralogical Association of Canada, Ottawa, Canada, pp. 99–145.

Cai, M.H., Han, F.B., He, L.Q., Chen, G.Q., Chen, K.X., Fu, J.M., 2008. He–Ar isotope characteristics and Rb–Sr dating of the Xintianling skarn scheelite deposit in South Hunan. China: Acta Geograph. Sin. 29, 167–173 (in Chinese with English abstract).

Clayton, R.N., Mayeda, T.K., 1963. The use of bromine pentafluoride in the extraction of oxygen from oxides and silicates for isotopic analysis. Geochim. Cosmochim. Acta 27, 43–52.
Cline, J.S., Bodnar, R.J., 1994. Direct evolution of brine from a crystallizing silicic melt at the Questa, New Mexico, molybdenum deposit. Econ. Geol. 89, 1780–1802.
Constantopoulos, J., 1988. Fluid inclusions and rare earth element geochemistry of fluorite from south-central Idaho. Econ. Geol. 83, 626–636.
Deng, S.F., 1997. Zoning regularity of mineral assemblages in the Huangshaping lead-zinc deposit. Mine. Resour. Geol. 11 (5), 314–318.
Fournier, R.O., 1987. Conceptual models of brine evolution in magmatic-hydrothermal systems. U.S. Geol. Surv. Prof. Pap. 1350, 1487–1506.
Fournier, R.O., 1991. The transition from hydrostatic to greater than hydrostatic fluid pressure in presently active continental hydrothermal systems in crystalline rock. Geophys. Res. Lett. 18, 955–958.
Gilder, S.A., Gill, J., Coe, R.S., 1996. Isotopic and paleomagnetic constraints on the Mesozoic tectonic evolution of south China. J. Geophys. Res. 101, 16137–16154.
Graf, A., 1997. Geology and Porphyry-Style Mineralization of the Cerro de la Gloria Stock Associated With High-T, Carbonate-Hosted Zn–Cu–Ag (Pb) Skarn Mineralization, San Martin District, Zacatecas, Mexico: Unpublished M.Sc. thesis. AZ, University of Arizona, Tucson, p. 163.
Graupner, T., Kempe, U., Dombon, E., 1999. Fluid regime and ore formation in the tungsten (−yttrium) deposits of Kyzyltau (Mongolian Altai): evidence for fluid variability in tungsten-tin ore systems. Chem. Geol. 154, 21–58.
Gu, L., 1997. On the genesis of the lead–zinc polymetallic deposit in Huangshaping. Hunan Geol. 16 (4), 232–238.
Hedenquist, J.W., Henley, R.W., 1985. The importance of $CO_2$ on freezing point measurements of fluid inclusions; evidence from active geothermal systems and implications for epithermal ore deposition. Econ. Geol. 80, 1379–1406.
Heinrich, C.A., 2005. The physical and chemical evolution of low salinity magmatic fluids at porphyry to epithermal transition: a thermodynamic study. Mineral. Deposita 39, 864–889.
Hoefs, J., Müller, G., Schuster, K.A., 1987. The Fe–Mn ore deposits of Urucum, Brazil: an oxygen isotope study. Chem. Geol. 65 (3–4), 311–319.
Hu, R.Z., Zhou, M.F., 2012. Multiple Mesozoic mineralization events in South China—an introduction to the thematic issue. Mineral. Deposita 47, 579–588.
Huang, G.F., 1999. Geological characteristics and seeking mineral orientation of Huangshaping style Pb–Zn deposit in Southern Hunan. Hunan Geol. 18, 84–115.
Huang, C., Li, X.F., Wang, L.F., 2013. Fluid inclusion study of the Huangshaping polymetallic deposit, Hunan province, South China. Acta Petrol. Sin. 29, 4232–4244.
Ishihara, S., Wang, P.A., Kajiwara, Y., Watanabe, Y., 2003. Origin of sulfur in some magmatic-hydrothermal ore deposits of South China. Bull. Geol. Surv. Jpn 54 (3/4), 161–169.
Jebrak, M., Smejkal, V., Albert, D., 1985. Rare earth and isotopic geochemistry of the fluorite–barite vein deposits from the western Rouergue District (France). Econ. Geol. 80, 2030–2034.
Jiang, S.Y., Zhao, K.D., Jiang, Y.H., Ling, H.F., Ni, P., 2006. New type of tin mineralization related to granite in South China: evidence from mineral chemistry, element and isotope geochemistry. Acta Petrol. Sin. 22, 2509–2516.
Klemm, L.M., Pettke, T., Heinrich, C.A., 2008. Fluid and source magma evolution of the Questa porphyry Mo deposit, New Mexico, USA. Mineral. Deposita 102, 1021–1045.
Lei, Z.H., Chen, F.W., Chen, Z.H., 2010. Petrogenetic and metallogenic age determination of the Huangshaping lead–zinc polymetallic deposit and its geological significance. Acta Geosci. Sin. 31, 532–540.
Li, S.J., 1997. A simple explanation to ore-controlling structure characters and ore-forming process analysis of Huangshaping Pb–Zn deposit in Hunan province. Geofis. Meteorol. 21 (4), 339–346.
Li, X.F., Sasaki, M., 2007. The hydrothermal alteration and mineralization of Middle Jurassic Dexing porphyry Cu–Mo deposit, Southeast China. Resour. Geol. 57, 409–426.
Li, X.F., Watanabe, Y., Hua, R.M., Mao, J.W., 2008. Mesozoic Cu–Mo–W–Sn mineralization and ridge/triple subduction in South China. Acta Geograph. Sin. 82, 625–640 (in Chinese with English abstract).
Li, X.F., Watanabe, Y., Yi, X.K., 2013a. Ages and sources of ore-related porphyries at Yongping Cu–Mo deposit in Jiangxi Province. Southeast China: Resour. Geol. 63, 288–312.
Li, X.F., Hu, R.Z., Brian, R., Xiao, R., Wang, C.Y., Yang, F., 2013b. U–Pb and Ar–Ar geochronology of the Fujiawu porphyry Cu-Mo deposit, Dexing district, Southeast China: Implications for magmatism, hydrothermal alteration, and mineralization. J. Asia Earth Sci. 74, 330–342.
Li, X.F., Hu, R.Z., Hua, R.M., Ma, D.S., Wu, L.Y., Qi, Y.Q., Peng, J.T., 2013c. The Mesozoic syntexis type granite-related Cu–Pb–Zn mineralization in South China. Acta Petrol. Sin. 29, 4037–4050 (in Chinese with English abstract).
Li, X.F., Wang, G., Mao, W., Wang, C.Z., Xiao, R., Wang, M., 2014a. Fluid inclusions, muscovite Ar–Ar age, and fluorite trace elements at the Baiyanghe volcanic Be–U–Mo deposit, Xinjiang, northwest China: Implication for its genesis. Ore Geol. Rev. 64, 387–399.
Li, J.G., Li, J.K., Wang, D.H., Liu, J., He, H.H., 2014b. The deep tectonic features of Qitianling ore concentrated area in Southern Hunan and its constraints to the regional ore-forming processes. Acta Geol. Sin. 88, 695–703.
Liu, W.H., Wang, L.M., Xu, W.X., 2005. Sulfur and lead isotope geochemical characteristics of the Huangshaping lead, zinc and silver polymetallic deposit. Acta Geosci. Sin. 26, 160–163.
Lu, Y.F., Ma, L.Y., Qu, W.J., Mei, Y.P., Chen, X.Q., 2006. U–Pb and Re–Os isotope geochronology of Baoshan Cu–Mo polymetallic ore deposit in Hunan Province. Acta Petrol. Sin. 22, 2483–2492.
Ma, T.Q., Wu, G.Y., Jia, B.H., 2005. Middle-late Jurassic granite magma-mixing in the middle segment of the Nanling Mountains, South China: evidence from mafic microgranular enclaves. Geological Bulletin of China vol. 24, pp. 506–512.
Ma, L.Y., Lu, Y.F., Mei, Y.P., Chen, X.Q., 2006a. Zircon SHRIMP U–Pb dating of granodiorite from Shuikoushan ore-field, Hunan Province, and its geological significance. Acta Petrol. Sin. 22, 2475–2482.
Ma, T.Q., Bai, D.Y., Kuang, J., 2006b. $^{40}Ar$–$^{39}Ar$ dating and geochemical characteristics of the granites in north Dadongshan pluton, Nanling Mountains. Geochimica 35, 333–345.
Ma, T.Q., Kuang, J., Bai, D.Y., 2006c. Geochemical characteristics and tectonic setting of the early Yanshanian South Zhuguangshan granite in the central segment of the Nanling Mountains. Geol. China 33, 119–131.
Ma, L.Y., Lu, Y.F., Qu, W.J., 2007. Re–Os isotopic chronology of molybdenites in Huangshaping lead–zinc deposit, southeast Hunan, and its geological implications. Mineral Deposits 26, 425–431.
Mao, J.W., Li, H.Y., Guy, B., Raimbault, L., 1996. Geology and metallogeny of the Shizhuyuan skarn-greisen W–Sn–Mo–Bi deposit, Hunan Province. Mineral Deposits 15, 1–15 (in Chinese with English abstract).
Mao, J.W., Li, X.F., Bernd, L., Chen, W., Lan, X.M., Wei, S.L., 2004. $^{40}Ar$–$^{39}Ar$ dating of tin ores and related granite in Furong tin ore-field, Hunan Province, and its ieodynamic significance. Mineral Deposits 23, 164–175 (in Chinese with English abstract).
Meinert, L.D., Hedenquist, J.W., Satoh, H., 2003. Formation of anhydrous and hydrous skarn in Cu–Au ore deposits by magmatic fluids. Econ. Geol. 98, 147–156.
Meinert, L.D., Dipple, G.M., Nicolescu, S., 2005. World Skarn Deposits: Economic Geology 100th Anniversary Volume. pp. 229–336.
Michard, A., 1989. Rare earth element systematics in hydrothermal fluids. Geochim. Cosmochim. Acta 53, 745–750.
Möller, P., Dulski, P., 1999. LA-ICPMS study of REE and Y distribution in fluorite. In: Stanley, C.J. (Ed.), Mineral Deposits: Processes to Processing: Rotterdam, Balkema, pp. 1133–1136.
Morozov, M., Trinkler, M., Plötze, M., 1996. Spectroscopic Studies on Fluorites From Li–F and Alkaline Granitic Systems in Central Kazakhstan: Granite-Related Ore Deposits of Central Kazakhstan and Adjacent Areas:. Global Publishing House, St Petersburg, pp. 359–369.
Ohmoto, H., Rye, R.O., 1979. Isotopes of sulfur and carbon. In: Barnes, H.L. (Ed.), Geochemistry of Hydrothermal Ore Deposits. John Wiley and Sons, New York, pp. 509–567.
Qi, F.Y., Zhang, Z., Zhu, X.Y., 2012. Skarn geochemistry of the Huangshaping W–Mo polymetallic deposit in Hunan and its geological significance. Geol. China 39, 338–348.
Roedder, J., 1984. Fluid Inclusions: Reviews in Mineralogy. pp. 1–644.
Sasaki, A., Ishihara, S., 1979. Sulfur isotope composition of the magnetite-series and ilmenite-series granitoids in Japan. Contributions to Petrology and. Mineralogy 68, pp. 107–115.
Shen, S., 1999. Ore matter composition and deposit factors-controlled of copper deposit in Huangshaping ore field. Hunan Geology 18, 75–78.
Sheppard, S.M.F., Gilg, H.A., 1996. Stable isotope geochemistry of clay minerals. Clay Miner. 31, 1–24.
Shi, M.K., Xiong, C.Y., Jia, D.Y., Lu, Y.F., Li, B., 1996. Comprehensive Prognosis for the Concealed Nonferrous Metallic Deposits in Hunan–Guangxi–Guangdong–Jiangxi Area. Geological Publishing House, Beijing, p. 142.
Shinohara, H., Hedenquist, J.W., 1997. Constraints on magma degassing beneath the Far Southeast porphyry Cu–Au deposit. Philipp.: J. Pet. 38, 1741–1752.
Sun, S.S., McDonough, W.F., 1989. Chemical and isotopic systematics of oceanic basalts: implications for mantle compositions and processes. In: Saunders, A.D., Norry, M.J. (Eds.), Magmatism in the Ocean Basins: London, Geological Society of London Special Paper. vol. 42, pp. 313–345.
Tong, Q.M., Jiang, S.Z., Li, R.Q., 1986. The characteristics of metallogeny of the Huangshaping lead-zinc ore deposit of Southern Hunan. Geol. Rev. 32, 565–577.
Trinkler, M., Monecke, T., Thomas, R., 2005. Constraints on the genesis of yellow fluorite in hydrothermal barite-fluorite veins of the Erzgebirge, Eastern Germany: evidence from optical absorption spectroscopy, rare-earth-element data, and fluid-inclusion investigations. Can. Mineral. 43, 883–898.
Ueda, A., Sakai, H., 1984. Sulfur isotope study of Quaternary volcanic rocks from the Japanese Islands Arc. Geochim. Cosmochim. Acta 48, 1837–1848.
Bodnar, R.J., Vityk, M.O., 1994. Interpretation of microthermometric data for $H_2O$–NaCl fluid inclusions. Fluid Inclusions in Minerals: Methods and Applications, pp. 117–130.
Wang, D.Z., Shen, W.Z., 2003. Genesis of granitoids and crustal evolution in Southeast China. Earth Sci. Front. 10, 209–220.
Wang, J.C., Yao, Y., Wang, K.Y., 1993. Study on feature of the associated silver mineralization in the Huangshaping lead–zinc deposit. Geol. Prospect. 29, 20–27.
Wang, Y.J., Fan, W.M., Guo, F., 2001. Petrological and geochemical characteristics of Mesozoic granodiorite intrusions in South east Hunan. Acta Petrol. Sin. 17, 169–175 (in Chinese with English abstract).
Wang, Y.L., Zhu, X.Y., Wang, L.J., 2010. Preliminary study on fluid characteristics of Huangshaping lead-zinc deposit. Hunan Province: Mineral deposits 29, 609–610.
Wu, G.Y., Ma, T.Q., Bao, D.Y., 2005. Petrological geochemical characteristics of granodiorite cryptoexplosion breccia and zircon SHRIMP dating in the Baoshan area, Hunan Province. Geoscience 19, 198–204 (in Chinese with English abstract).
Xi, C.Z., Dai, T.G., Liu, W.H., 2009. Lead and sulfur isotope geochemistry of the Huangshaping lead–zinc deposit, Hunan province. Acta Geosci. Sin. 30, 89–94.
Xie, C.Y., Lu, J.J., Ma, D.S., Zhang, R.Q., Gao, J.F., Yao, Y., 2013. Origin of granodiorite porphyry and mafic microgranular enclave in the Baoshan Pb–Zn polymetallic deposit, South Hunan Province: Zircon U-Pb chronological, geochemical and Sr-Nd-Hf isotopic constraints. Acta Petrol. Sin. 29, 4186–4214.
Yang, M.G., Huang, S.B., Lou, F.S., Tang, W.X., Mao, S.B., 2009. Lithospheric structure and large-scale metallogenic process in Southeast China continental area. Geol. China 36, 528–543.
Yao, J.R., Wang, J.H., Cao, Y.Z., 1993. The deep structures in Hunan. Geol. Hunan S7, 1–100.

Yao, J.M., Hua, R.M., Lin, J.F., 2005. Zircon LA-ICPMS U–Pb dating and geochemical characteristics of Huangshaping granite in Southeast Hunan Province. China: Acta Petrol. Sin. 21, 688–696.
Yao, J.M., Hua, R.M., Qu, W.J., 2007. Re–Os isotope dating of molybdenites in the Huangshaping Pb–Zn–W–Mo polymetallic deposit, Hunan Province, South China and its geological significance: Science in China Series D. Earth Sci. 50, 519–526.
Yao, J.R., Xiao, H.Y., Liu, Y.R., Bao, D.Y., Deng, Y.L., 2012. Location of the Yangtze–Cathaysia plate convergence zone in Hunan. Chin. J. Geophys. 55, 484–502.
Yuan, Y.B., Yuan, S.D., Chen, C.J., Huo, R., 2014. Zircon U–Pb ages and Hf isotopes of the granitoids in the Huangshaping mining area and their geological significance. Acta Petrol. Sin. 30, 64–78.
Yuang, Y.B., Yuan, S.D., Liu, X.F., Zhang, J.R., 2013. Sulfur isotopic characteristics of the granitoids in the Huangshaping mining area and their geological significance. Acta Geol. Sin. 88 (12), 2437–2442.
Zeng, Z.X., 2001. Geological characteristics and genesis of the copper deposit of the Huangshaping ore field. Hunan Nonferrous Metals vol. 17, pp. 8–10.
Zhai, Y.S., Deng, J., Li, X.B., 1999. Essentials of Metallogeny: Beijing, Geological Publishing House. p. 224 (in Chinese with English abstract).
Zhang, J.X., Tong, Q.M., Li, R.Q., 2000. Regional geochemical characteristics across the Chenzhou-Linwu deep-seated fault. Geol. Miner. Resour. South China 3 (p. 17–14 in Chinese with English abstract).
Zhang, Z., Wang, J.B., Qi, F.Y., 2012. The C–O–S–Pb isotopes at the Huangshaping polymetallic deposit, Hunan Province. China: Acta Mineral. Sin. 35, 433–444.
Zheng, Y.F., 1993. Calculation of oxygen isotope fractionation in hydroxyl-bearing silicates. Earth Planet. Sci. Lett. 120, 247–263.
Zhong, Z.C., 1996. Magma rocks and their ore-controlling characteristics in the Huangshaping mining area. Geophys. Prospect. 10, 400–405.
Zhou, T.F., Yue, S.C., 1996. Isotope geochemistry of copper mineralization in Yueshan, Anhui. Mineral Deposits 15 (4), 341–350 (in Chinese with Englishabstract).
Zhu, E.J., Wang, J.G., and Qiu, Y.M., 1995, The distribution regularity and occurrence of the associated silver in the Huangshaping Pb–Zn ore filed, Hunan province: Geological exploration for non-ferrous metals, vol. 4, p. 89–95.
Zhu, X.Y., Wang, J.B., Zhang, Z., Wang, Y.L., Jiang, Y.C., 2010. Identification of the NNW trending ore-controlling structure in the Huangshaping lead–zinc deposit, Hunan Province and its significance to exploration. Geophys. Prospect. 46, 609–661.
Zhu, X.Y., Wang, J.B., Wang, Y.L., Cheng, X.Y., Fu, Q.B., 2012. Sulfur and lead isotope constraints on ore formation of the Huangshaping W–Mo–Bi–Pb–Zn polymetallic ore deposit, Hunan Province, South China. Acta Petrol. Sin. 28, 3809–3822.